Received: 23 August 2024 | Revised: 16 September 2024 | Accepted: 20 September 2024

DOI: 10.1096/fj.202401977R

RESEARCH ARTICLE

The FASEB Journal

Emc1 is essential for vision and zebrafish photoreceptor outer segment morphogenesis

Tess McCann[1,2] | **Husvinee Sundaramurthi**[1,2] | **Ciara Walsh**[1,2] | **Sanamjeet Virdi**[3,4] | **Yolanda Alvarez**[1,2] | **Beata Sapetto-Rebow**[1,2] | **Ross F. Collery**[1,2,5] | **Stephen P. Carter**[1,2] | **Ailis Moran**[1,2] | **Ruth Mulholland**[1,2] | **John J. O'Connor**[1,2] | **Michael R. Taylor**[6] | **Nora Rauch**[2] | **Margaret R. Starostik**[7] | **Milton A. English**[7] | **Anand Swaroop**[7] | **Robert Geisler**[3] | **Alison L. Reynolds**[2,8] | **Breandán N. Kennedy**[1,2]

[1]UCD School of Biomolecular and Biomedical Science, University College Dublin, Dublin, Ireland

[2]UCD Conway Institute of Biomolecular and Biomedical Sciences, University College Dublin, Dublin, Ireland

[3]Karlsruhe Institute of Technology (KIT) Institute of Biological and Chemical Systems -Biological Information Processing, Eggenstein-Leopoldshafen, Germany

[4]Leibniz Institute of Virology (LIV), Hamburg, Germany

[5]Medical College of Wisconsin Eye Institute, Milwaukee, Wisconsin, USA

[6]School of Pharmacy, University of Wisconsin-Madison, Madison, Wisconsin, USA

[7]Neurobiology, Neurodegeneration & Repair Laboratory, National Eye Institute, National Institutes of Health, Bethesda, Maryland, USA

[8]School of Veterinary Medicine, Veterinary Science Centre, University College Dublin, Dublin, Ireland

Correspondence
Breandán N. Kennedy, F053 UCD Conway Institute, University College Dublin, Belfield, Dublin 4, Ireland.
Email: brendan.kennedy@ucd.ie

Funding information
Science Foundation Ireland (SFI), Grant/Award Number: 20/FFP-P/8538 and 04/IN3/B559; National Eye Institute, Grant/Award Number: Z01EY000450; Marie Skłodowska-Curie Actions, Grant/Award Number: 666010

Abstract

Inherited retinal diseases (IRDs) are a rare group of eye disorders characterized by progressive dysfunction and degeneration of retinal cells. In this study, we characterized the *raifteirí (raf)* zebrafish, a novel model of inherited blindness, identified through an unbiased ENU mutagenesis screen. A mutation in the largest subunit of the endoplasmic reticulum membrane protein complex, *emc1* was subsequently identified as the causative *raf* mutation. We sought to elucidate the cellular and molecular phenotypes in the *emc1*$^{-/-}$ knockout model and explore the association of *emc1* with retinal degeneration. Visual behavior and retinal electrophysiology assays demonstrated that *emc1*$^{-/-}$ mutants had severe visual impairments. Retinal histology and morphometric analysis revealed extensive abnormalities, including thinning of the photoreceptor layer, in addition to large gaps surrounding the lens. Notably, photoreceptor outer segments were drastically smaller, outer segment protein expression was altered and hyaloid

---

Abbreviations: cpd, cycles per degree; dpf, days post fertilization; EMC, endoplasmic reticulum membrane protein complex; EMC1, endoplasmic reticulum membrane protein complex subunit 1; IRD, inherited retinal disease/dystrophy; OS, outer segment.

The FASEB Journal. 2024;38:e70086.
https://doi.org/10.1096/fj.202401977R

vasculature development was disrupted. Transcriptomic profiling identified cone and rod-specific phototransduction genes significantly downregulated by loss of *emc1*. These data shed light on why *emc1* is a causative gene in inherited retinal disease and how outer segment morphogenesis is regulated.

KEYWORDS

emc1, endoplasmic reticulum, inherited retinal disease, outer segment, photoreceptor, phototransduction, unfolded protein response, vasculature, zebrafish

1 | INTRODUCTION

Inherited retinal diseases/dystrophies (IRDs) are a diverse array of eye diseases often caused by genetic mutations disrupting the function of photoreceptors.[1] Currently, over 304 genes are linked to IRDs (https://retnet.org/summaries#d-graph, Oct 2024) but many of the underlying mechanisms of the disease remain unknown. This contributes to the very limited treatments available for IRD patients; with only one approved gene therapy. The photoreceptor outer segment (OS) is a specialized sub-region for the detection of light and initiation of phototransduction. A subset of IRD genes are linked to defective OS morphogenesis. Generating and characterizing new *in vivo* models of IRD and defective OS morphogenesis provides opportunities to examine the biology of retinal disease and opens potential therapeutic avenues.

The photoreceptor OS is a highly modified primary cilium[2] whose OS discs or lamellae are packed with proteins enabling the phototransduction cascades needed for light perception.[3] Phototransduction leads to the production of photooxidative byproducts, so the OS must undergo constant renewal and recycling for vision to be maintained.[4] This leads to a continuous demand for new proteins to be translated, modified, and transported to the OS correctly. Mutations in genes that cause a disruption anywhere along this process can cause photoreceptor dysfunction, and subsequent degeneration ultimately leading to blindness.[5]

The zebrafish is a powerful vertebrate model organism in genetic and developmental biology. Their size, rapid eye development, cone-rich retina, and diurnal behavior make them extremely amenable to studying ocular diseases.[6–8] Using these advantages, we performed an unbiased forward genetic screen to discover novel gene variants causing impaired vision. We identified a recessive lethal mutation, initially named *raifteirí (raf)* that causes a severe decrease in visual behavior and function. We further investigated the cellular phenotypes present in the *raf* mutants and discovered a selective defect in photoreceptor appearance and structure, particularly OS development.

Whole genome and RNA sequencing identified the gene responsible for the *raf* phenotype as endoplasmic reticulum membrane complex subunit 1 (*emc1*). The *emc1* gene is a part of the EMC (Endoplasmic Reticulum Membrane Complex), which acts as a modulator of multipass membrane proteins,[9–11] an insertase for transmembrane domains of multiple tail-anchored (TA) proteins[12] and G-protein coupled receptors (GPCRs).[13] These processes are essential for maintaining the morphology and function of the OS. EMC1 has been associated with human retinitis pigmentosa and neurodevelopmental disorders.[14–16] However, the specific mechanisms by which *EMC1* mutations lead to these phenotypes remain poorly understood. Our *raf* zebrafish model is a novel way to investigate the role of *emc1* in vertebrate development and its potential implications in human disease. This novel model allows for the in vivo examination of the developmental processes influenced by *emc1*, as well as the cellular and molecular consequences of its dysfunction.

Here, we present our findings on the phenotypic characterization of zebrafish *raf* mutants. In all visual behavior assays, the *raf* mutants displayed severely decreased responses. Analysis of retinal morphology revealed a selective attenuation of photoreceptor OS morphogenesis and an irregular hyaloid vasculature. We hypothesized that OS proteins would be dysfunctional in *raf* mutants and discovered that proteins enriched in OS, such as Rab28 and Peripherin 2, had altered expression or localization. Finally, transcriptomic analysis was performed to identify the downstream consequences of the loss of *emc1* and it was determined that the expression of phototransduction genes was significantly downregulated. Our study sheds light on the critical roles of *emc1* in vision and provides a foundation for understanding the broader implications of its dysfunction.

2 | METHODS

2.1 | Zebrafish maintenance and husbandry

All animal experiments were carried out at University College Dublin and approved by the University College Dublin Animal Research Ethics Committee (AREC).

Embryos were generated by matings from natural spawning, and raised until 131 hpf in an incubator at 27°C in Petri dishes of E2 embryo medium (0.137 M NaCl, 5.4 mM KCl, 5.5 mM Na_2HPO_4, 0.44 mM KH_2PO_4, 1.3 mM $CaCl_2$, 1.0 mM $MgSO_4$, and 4.2 mM $NaHCO_3$, conductivity ~1500 μS) containing methylene blue (Sigma Aldrich, UK). Adult zebrafish were maintained in a 14-h light, 10-h dark cycle on an Aquatic Habitats (Florida, USA) recirculating filter water system (28°C, pH 6.8–7.5). Larval zebrafish were fed pellet food (SDS, Special Diet Services, 100) and paramecium up to 14 days post fertilization (dpf), and SDS 200 and live brine shrimp (*Artemia* sp.) up to 28 dpf. Juvenile and adult zebrafish were fed a combination of live brine shrimp and pellet food (SDS 400) twice daily. Zebrafish strains used in this study were as follows: *raf* ENU, *raf*;*Tg(gnat2:eGFP-Rab28*^{wt}*)* and *raf*;*Tg(fli1:EGFP)*.

2.2 | ENU mutagenesis

Zebrafish males of AB strain (RRID:ZIRC_ZL1) were mutagenized with N-ethyl-N-nitrosourea (ENU) and mated to wild-type (Tübingen, RRID:ZIRC_ZL57) females to generate F1 founder fish. F1 founders were mated to wild-type fish to establish F2 families. F3 offspring of random incrosses within F2 families were screened for defects in visual behavior by 131 hpf. 25% of the offspring from heterozygous carriers presented with *raf* phenotypes.[17]

2.3 | Optokinetic response

To measure the optokinetic response (OKR), zebrafish larvae were immobilized in a 60 mm Petri dish containing pre-warmed 9% methylcellulose and placed in the center of a rotating drum containing black and white stripes. Standard OKR analysis employed 100% black contrast (bc) and 20 stripes (1 cm width, 0.02 cycles per degree [cpd]). Contrast sensitivity analysis was performed using 20% bc stripes (0.02 cpd). Visual acuity was assessed by reducing the stripe width (0.2 cpd, 100% bc). Colored pattern analysis (Red-Green-Blue; RGB) involved 0.02 cpd drums of alternating black-green, black-red, or black-blue stripes. The light source was a Zeiss KL1500 LCD set at 22.7% power. Each drum was rotated at 18 rpm for 30 s in a clockwise direction, then 30 s counter-clockwise. Saccades were recorded manually using a microscope focused on the eyes while the drum rotated.[18] All OKR measurements were performed between the hours of 11 am and 2 pm to maintain experimental consistency and prevent diurnal variations.[19]

2.4 | ERG

The electroretinogram (ERG) was recorded on 6 dpf larvae as previously described.[20] Briefly, zebrafish were dark adapted for a minimum of 20 min, paralyzed with 0.5 mg/mL mivacurium chloride (Mivacron®), and pipetted into the recording dish containing a piece of damp sponge covered in filter paper. Each larva was placed in lateral orientation with the right eye facing upward and the trunk covered with damp tissue to prevent desiccation. All recordings took place in the afternoon/early evening. The recording electrode, a thick-walled glass capillary (tip diameter: 80–100 μm) containing 0.9% saline, was placed on the right cornea. The reference electrode, a bleached silver/silver chloride wire, was placed underneath the filter paper on top of the sponge. The voltage signal was amplified using a differential P55 pre-amplifier (Grass Instruments) with a bandpass of 0.1 and 100 Hz. A 50-Hz line filter was switched on to remove cyclical noise. The larva was left for 2 min in situ prior to recording. A 300-W tungsten light source was used for stimulus and an LED light source for background light. The unattenuated irradiances for the background and the stimulus were 50 μW/cm^2 and 2.8×10^3 μW/cm^2, respectively. Stimulus flash duration was controlled by a mechanical shutter (Newport Corporation) and the rate was controlled by an S48 stimulator (Grass Instruments). Data were acquired using a PC with a NiDAQ 6024E board, running Windows Whole Cell Program (WinWCP, University of Strathclyde). Full-field white flashes (500 milliseconds (ms)) were presented every 30 s to the dark-adapted eye. The data were signal averaged (5–10 signals). For all recordings, flashes attenuated by 2.0, 1.0, and 0 (unattenuated) log units were used. The amplitude of the various waves was measured as described previously.[21]

2.5 | Diurnal locomotor activity

The diurnal locomotor activity (average seconds activity per minute) of *raf* mutants and their wild-type siblings were recorded over 42 h, using the Viewpoint Zebrabox system, from the evening of 4 dpf to the morning of 6 dpf. An assessment was made of the average activity levels (sec/min) over the entire experiment (all), during the night time (dark) and during the day time (light). Following this experiment, larvae were phenotyped using OKR.

2.6 | Visual motor response

To measure the visual motor response (VMR), individual 5 dpf larvae were placed in a polystyrene 96-well plate in 600 µL of embryo medium, which was placed in a Zebrabox recording chamber (Viewpoint Life Sciences, France) to record locomotor activity in milliseconds per second (ms/s). The detection sensitivity was set to 20, the activity burst threshold set to 25, and the activity freeze threshold set to 5. Larvae were acclimatized for 30 min, followed by 100 min with lights switching on and off in 20-min intervals.[18] The activity for each fish was calculated from the sum of its activity above the freeze threshold (middle duration and burst duration). The activity for each fish across both light OFF periods (3000–4199 s, 5400–6599 s) or both light ON periods (4200–5399 s, 6600–7799 s) was averaged. The peak of activity immediately after the light OFF/ON was calculated by averaging the activity for each fish during the 10s before and after the light OFF (2990–3010 s, 5390–5410 s) and light ON (4190–4210 s, 6590–6610 s). The Max-ON and Max-OFF values were calculated from the average light OFF and light ON values by finding the maximum activity of each fish during the 5 s (0–4 s) after the light change.

2.7 | Fluorescence microscopy

Whole larvae were fixed overnight in 4% PFA. The following day, samples were washed three times for 5 min with 1X PBS, before being soaked in a sucrose series as previously described.[22] For cryosectioning, cryomolds were filled with OCT (VMR/Cell Path) at room temperature. Up to 5 larvae in a block were lined up and embedded. Cryomolds were stored until processing at −80°C. Samples were cut into 12–20 µm sections using a cryostat (Leica CM1860/CM1860 UV) onto super-frost slides and dried overnight. The next day they were rehydrated with 1X PBS. Sections were incubated in blocking buffer (2% normal goat serum, 1% bovine serum albumin, 1% triton X-100 in PBS) for at least an hour at room temperature. Primary antibodies were diluted in blocking buffer applied to the sections and placed at 4°C overnight. Sections were washed three times with PBST and incubated in secondary antibodies diluted in blocking buffer for at least 1 h at room temperature. To label different cell populations, the following primary antibodies were used: 4C12 (1:20; J. Fadool, unknown epitope in rod plasma membrane), 1D1 (1:200; J. Fadool, rhodopsin), Zpr3 (1:200, ZIRC, RRID:AB_10013805, rod outer segment), zpr1 (1:200, ZIRC,rrid/RRID:AB_10013803, cone cytoplasm), lectin-PNA (1: 100, ThermoFisher, cone OS) PKC-alpha (1:200; M. Ader), UW-55-anti-CRALBP (1:500; J. Saari, Müeller glia), and SV2 (1:500; DSHB, synaptic vesicles). To label different parts of the photoreceptor, the following primary antibodies were used: peripherin2 (1:100, proteintech #18109-1-AP, RRID:AB_10665364), gnb3 (1:100, proteintech #10081-1-AP, RRID:AB_2263264), and centrin (1:200, Sigma aldrich ZMS1054). Finally, sections were counterstained with DAPI or Hoechst 33342 (1:1000). Aqua/Polymount was placed on the sections and coversliped. To image the GFP reporters in the mutant background GFP positive larvae were selected and processed by cryosectioning. For *Tg(gnat2:rab28-eGFP)* analysis, a total of 10 and 9 individuals, for sibling and *raf*, respectively, were imaged. For imaging, z-stacks were taken using a Zeiss LSM510/LSM 800 Airy confocal microscope (Carl Zeiss, Germany).

For vessel analysis, sibling and raf larvae in the *Tg(fli1:EGFP)* background (RRID:ZIRC_ZL1085) were screened for GFP and fixed at 131 hpf in 4% PFA fixative overnight at 4°C. Samples were washed three times the next day in 1X PBS before enucleation of the eyes and lens dissection was performed using an Olympus SZX16 fluorescent microscope to visualize. For analysis, lenses were transferred onto microscope depression slides containing 9% methylcellulose and reorientated with tweezers for visualization and imaging of the hyaloid blood vessels using Olympus CellSens Standard software (Olympus, Japan).

2.8 | Transmitted light microscopy

131 hpf larvae were fixed in 2.5% glutaraldehyde, 2% paraformaldehyde (PFA), and 0.1% 0.2 M Sorenson's phosphate buffer (pH 7.3) in glass vials at 4°C, and left for a minimum of 48 h. Sorensen's buffer (0.1 M) was used to wash the samples before transfer to 1% osmium tetroxide (Sigma Aldrich, UK) for 1 h. The samples were then dehydrated with an ethanol gradient (30%, 50%, 70%, 90%, and 100%). 50 mL of resin was made using 24 g Agar 100, 9.5 g dodecenylsuccinic anhydride (DDSA), 16.5 g methyl nadic anhydride (MNA), and 1 g of dimethyl pimelimidate-30 (DMP-30). The EPON mixture was left to stir for 20 min at 250 rpm for thorough mixing. The samples were then washed with propylene oxide (Sigma Aldrich), and individual larvae were embedded in 1 mL of agar epoxy resin (EPON: propylene oxide 1:1) at 60°C overnight in a mold, and 1 µm sections were acquired using a Leica EM UC6 ultramicrotome. Sections were mounted on glass slides stained with toluidine blue, and imaged using 40x lens with a Nikon Eclipse 80i transmitted light microscope equipped with a Canon EOS 600D camera. Image and morphometric analysis were performed using Image J (https://imagej.net/, RRID:SCR_003070). For quantitative measurement of central retinal layers, images of the whole eye were confirmed to contain the optic nerve, orientated, and a straight line connecting both marginal

zones (frontal plane; FP) was traced. Then, a perpendicular line to the frontal plane was traced from the lens to the RPE, named the optical axis (OA). All retinal layers were measured along the OA.

2.9 | Transmitted electron microscopy

Zebrafish larvae were embedded for TEM using the same protocol as for light microscopy. 80 nm sections were cut on a Leica EM UC6 microtome, mounted on copper grids, and post-stained with 2% uranyl acetate and 3% lead citrate. Imaging was performed on an FEI-Tecnai 120 BioTwin electron microscope (FEI electron optics).

2.10 | Whole genome and RNA Sequencing

DNA was isolated from 20 *raf*$^{-/-}$ or wild-type sibling larvae (sorted according to larvae with and without an inflated swim bladder) at 5 dpf using the Qiagen tissue extraction kit. Samples were outsourced to Novogene for whole genome sequencing. Positional cloning and mutation mapping of the *raf* mutation utilized a custom algorithm.[23] For RNA sequencing, RNA was isolated from ~80 *raf*$^{-/-}$ or sibling's eyes at 5 dpf (phenotyped according to the presence of an inflated swim bladder) using the MirVana Kit (ThermoFisher, AM1560). Each replicate contained 80 eyes from 40 larvae, in total five biological replicates for sibling and *raf*$^{-/-}$ were collected. RNA quality was evaluated using the Bioanalyzer 2100 6000 Nano assay (Agilent Technologies), confirming that the RNA Integrity Number (RIN) was >9 for each sample. Sequencing libraries were prepared using the TruSeq® Stranded mRNA Library Preparation kit (Illumina) and sequenced on the Illumina HiSeq 2500 platform. Raw reads were trimmed for Illumina adapters using Trimmomatic version 0.36.[24] Quality control checks were performed using FastQC version 0.11.5 (http://www.bioinformatics.babraham.ac.uk/projects/fastqc/) and MultiQC version 1.5.[25] Of the 10 pools, pools were excluded if general information from the pool was inconsistent with subject descriptors (0) or if pools failed to meet any aforementioned quality control metrics (0). The entire QC process yielded 10 high-quality pools for analysis (5 wild-type siblings and 5 *raf*$^{-/-}$ mutants). Trimmed reads were aligned to the GRCz11 Danio rerio genome from NCBI using STAR version 2.5.2a[26] with per-sample 2-pass mapping and ENCODE standard options. The mean number of uniquely mapped paired-end reads per pool was 36.09 ± 3.84 million (range 32.97–46.02 million) with a mean total mapping rate of 92% to the reference genome assembly. Transcript-level abundances were quantified using Kallisto version 0.43.0[27] and summarized into gene-level abundances using Tximport version 1.6.0[28] in R (http://www.r-project.org/index.html). Differential gene expression analysis between *raf*$^{-/-}$ and wildtype was performed using the limma package[29] in R with a significance threshold of FDR ≤0.05. First, lowly expressed genes were removed by applying an expression threshold of at least 2 CPM in at least 3 of the 5 pools for each treatment (i.e., wildtype and *raf*$^{-/-}$), retaining 17 244 genes for analysis. Batch effects were estimated using surrogate variable analysis (SVA).[30] All 3 significant covariates estimated by SVA were included in the differential expression analysis. As a quality control check, we performed principal component analysis on normalized data. Normalization was performed using Trimmed Mean of M-values (TMM) in Counts per Million (CPM) using edgeR version 3.18.1.[31–33] Normalized values were subsequently converted into log2 CPM with an offset of 1. We applied MMAPPR[34] to identify the causative mutation underlying the *raf* phenotype.

2.11 | Pathway enrichment analysis

Differential gene expression analyses were performed from the bulk RNA sequencing data using the RNAlysis interface (https://guyteichman.github.io/RNAlysis/build/index.html); FASTQ reads were aligned to Zebrafish GRCz11 with Kallisto and read counts for each sample was found. Read counts were filtered (removal of genes that were not detected in all samples, sibling only or *raf* only) and differential analysis was performed with DESEq2 to compare siblings to *raf* samples. The list of differentially expressed genes was filtered for adjusted p values <.05 and Log2 fold change >1 or −1. These downregulated or upregulated DEGs were then converted from Ensembl IDs to gene name and Entrez IDs using Biomart (https://www.ensembl.org/biomart/martview/d65138581000520fcdce0c5235e9a160). The Entrez IDs were then uploaded as gene lists to DAVID (https://david.ncifcrf.gov/tools.jsp) and ShinyGo (http://bioinformatics.sdstate.edu/go/) to find the enriched GO terms and KEGG pathways.

2.12 | Genotyping larvae and adults

raf$^{-/-}$ zebrafish are identified by lack of swim bladder from 5 dpf. Once a mutation has been identified in *emc1*, a subset of larvae was sent for Sanger sequencing from extracted genomic DNA to confirm the homozygosity of the SNP in exon 4 of *emc1*. Heterozygous adult zebrafish are identified through genomic DNA extracted from fin clips. Sequences of primers used for genotyping were emc1_genotyping_forward: TGTTCTTGGTTTCGTGCAGG and emc1_genotyping_reverse: GCACAGCAACGTACTTCACA, expected size = 504 bp.

2.13 | Quantitative PCR

For qPCR experiments, 5 dpf larvae were collected in tubes containing 10–20 larvae per tube, and stored in RNALater (Sigma). The pools of whole larvae were homogenized through a 26-gauge needle/syringe and total RNA was extracted using TRIzol (ThermoFisher Scientific). RNA was precipitated with phenol-chloroform and resuspended in nuclease-free water. The total RNA concentration and integrity (260/280) were quantified using the DeNovix DS-11 Series Spectrophotometer, and samples were stored at −80°C to prevent degradation until further use. RNA was treated with DNase (AMPD1, Sigma-Aldrich). cDNA was synthesized from 500 ng of total RNA using the PrimeScript™ RT reagent kit (Perfect Real Time, TAKARA, Japan). Quantitative real-time PCRs were carried out using a QuantStudio 7 Flex Real-Time PCR System (Applied Biosystems). Targets were detected using PowerSYBR Green PCR Master Mix (Applied Biosystems) under the following conditions: 50°C for 2 min, 95°C for 10 min, then 40 cycles at 95°C for 15 s and 60°C for 60 s. Results were analyzed using Quantstudio Real-time PCR software. All reactions were performed in technical triplicates. Relative expression of targets was assessed by the 2-ΔΔCT method using β-actin as the housekeeping gene. Primers that spanned across exons for each target gene were designed using Primer3. Primer sequences used and expected product sizes are shown in Table 1.

2.14 | Statistics and data analysis

Statistical analysis was performed using GraphPad Prism™ v.9 software (GraphPad, San Diego, CA). Details of tests used can be found in figure legends. Significance levels were set at $p < .05$.

3 | RESULTS

3.1 | F3 Mutagenesis Screen Identification of *raf*, a novel zebrafish model of Inherited Blindness

During an F3 N-ethyl-N-nitrosourea (ENU) mutagenesis screen to identify zebrafish with inherited visual behavior impairments, the *raifteirí* (*raf*) mutant line was uncovered. The gross morphology of $raf^{-/-}$ larvae is largely unaffected beside the absence of inflated swim bladders (Figure 1A). This feature is commonly observed in visually compromised zebrafish.[35,36] The primary phenotype in $raf^{-/-}$ was severely impaired visual behavior measured by larval optokinetic response (OKR) assays. The OKR measures saccadic eye movements in response to a rotating striped drum.[19] OKR analysis performed under standard conditions (100% black contrast, 0.02 cpd drum), revealed an essentially absent (>99% reduction) saccadic response ($p < .0001$) of $raf^{-/-}$ larvae, averaging 0 saccades per minute, compared to wild-type siblings, averaging 17.2 saccades per minute (Figure 1B). It was concluded that $raf^{-/-}$ is a model of recessive inherited blindness with ~25% of the total offspring displaying uninflated swim bladders and abnormal OKR.

Further assessment of the visual behavior defects used variations in the OKR drum to assess responses to drums

TABLE 1 The DNA sequences of the forward and reverse primers used to amplify each gene in quantitative PCR. The expected product size is shown.

gene	Forward (5′–3′)	Reverse (5′–3′)	Product size
actb1	CTTCCTGGGTATGGAATCTTGC	GTGGAAGGAGCAAGAGAGGTG	177
emc1	GGCAACAGTACATCGGCAAG	TTGTATCAGCTGGCATTGCC	149
emc3	CCCTGATTCTTGGACAGGAT	TTGTATCAGCTGGCATTGCC	93
axin2	CTCGGACACTTCAAGGAACAAC	ATTGGCAGAACTGTGCAGTC	128
isg15	GGTGATGCTACCGTTGGAAT	CTGAGGGTCCGGGATTCATC	128
fosl1a	ATGAATCCTCCTCAGCCCTC	CAGCCATTTTGTTGCGTTCC	157
irg1l	CGGGCTTGACTTTCTAACCG	CATTACTGGCTTGGTTGCGA	182
fga	AGATTCGACGTCTCCTGGTG	GTCCAGAAGTCGAAGTTGGC	200
rhol	TACTTGGCATCTCCGTTTGC	ATATAGTTCAGAGGCGTCCG	137
pth1b	TTGTGCTGTGGAGTCTTTGC	TTGTGCTCCCGAACATTGTG	104
pde6ga	CCAAGCCTAAATCGACCAGC	TCCCAATCCCTCCATTCCAG	171
gnat1	GGACCGTCAAACTTCTGCTG	TCCAAGCACTCTTCAAGGGA	109

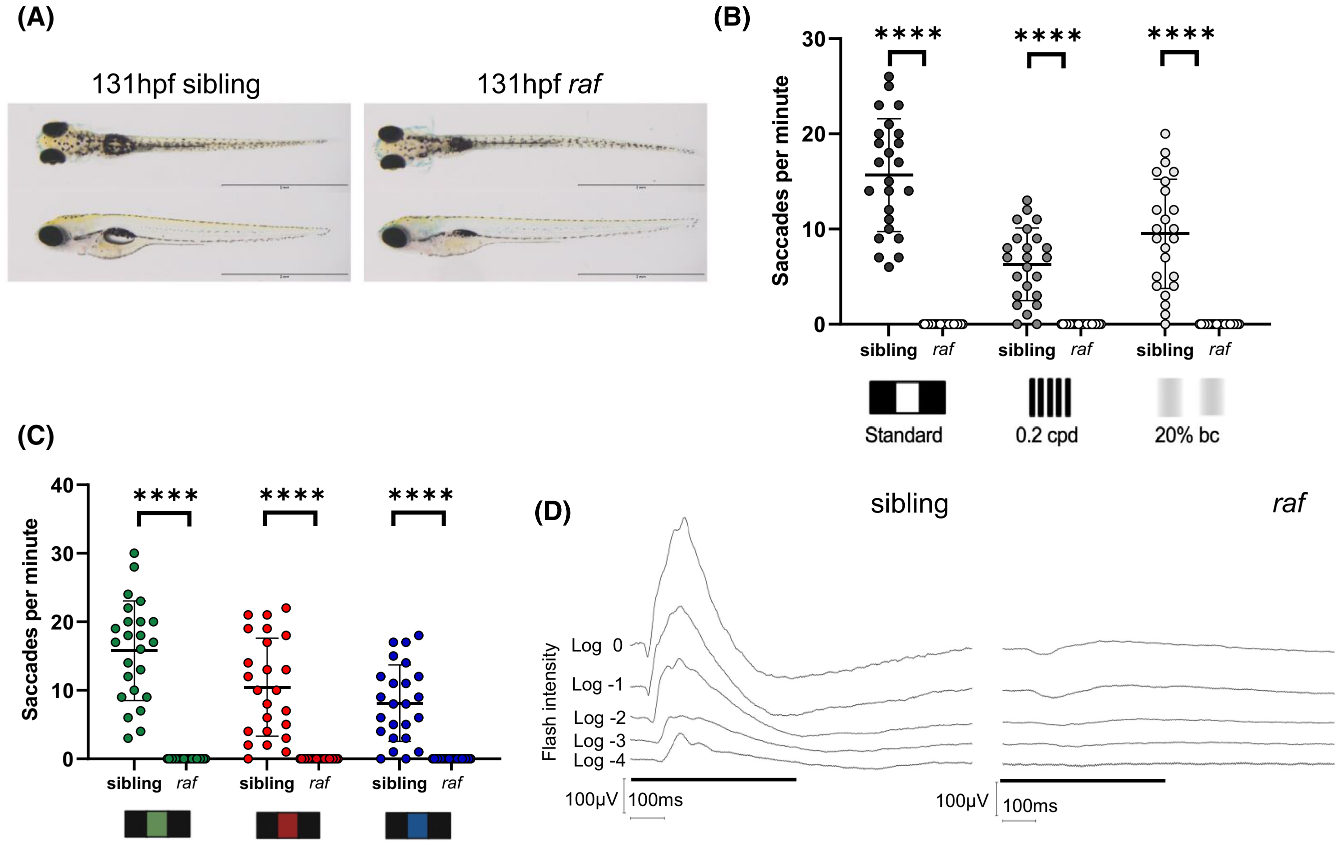

FIGURE 1 *raf* is a novel zebrafish model of inherited blindness. (A) Gross morphology of *raf* mutant larvae and sibling controls at 131 hpf. Mutants lack an inflated swim bladder but have otherwise normal gross morphology. Scale bar = 2 mm. (B) Visual behavior was assessed by different OKR drums; standard, 0.2 cpd (cycles per degree) and 20% black contrast (bc) in <131 hpf larvae. (C) Visual behavior was assessed by sequential exposure to colored standard OKR drums. $N=3$ independent biological replicates with $n=8$ larvae per replicate. Error bars indicate the mean ± SD. The midline of the error bars represents the group average. A non-parametric Mann–Whitney U-test was performed where $^{****}p<.0001$. (D) Analysis of visual function measured by electroretinogram. The response of the outer retina to a short (500 ms, rectangular black bar) flash of light at 5 increasing intensities of light ($0 \log = 2.8\times10^3$ μW/cm^2) was recorded at the corneal surface of 6 dpf zebrafish larvae. $n=5$ (sibling), 6 (*raf* mutants).

with thinner stripes, less contrast between stripes, or various colored patterns (Figure 1B,C). Compared to siblings, *raf*$^{-/-}$ displayed virtually absent OKR saccades to a 100% contrast striped drum with 0.2 cpd, used to test visual acuity, or a 20% black contrast drum with 0.02 cpd, used to test contrast sensitivity.[19] *raf*$^{-/-}$ showed an average of 0 saccades per minute for both drums whereas siblings showed an average of 6.3 saccades per minute for the visual acuity drum and 9.5 saccades per minute for the contrast sensitivity drum (Figure 1B). Likewise, *raf*$^{-/-}$ responses to drums with colored stripes showed an average of 0 saccades per minute, while in contrast, the siblings displayed an average saccade per minute of 10.5 for the red-black drum, 8.1 for the blue-black drum, and 15.8 for the green-black drum (Figure 1C). Collectively, OKR results for the *raf* mutant when exposed to varying stimuli confirmed severely impaired vision.

To assess retinal function, electroretinography (ERG) was performed. Figure 1D shows the response of the outer retina to a 500 ms flash of increasing light intensity ($0 \log = 2.8\times10^3$ μW/cm^2) recorded at the corneal surface of 6 dpf *raf*$^{-/-}$ and siblings, previously phenotyped by OKR. The ERG of the OKR-positive siblings displays a normal max a-wave amplitude of −35 ± 14 μV occurring at 91 ± 40 ms and a normal max b-wave amplitude of 236 ± 141 μV occurring at 271 ± 88 ms ($n=4$). In contrast, the ERG of the OKR-negative *raf*$^{-/-}$ is severely diminished and delayed, with a max a-wave amplitude of −18 ± 12 μV delayed to 147 ± 47 ms and a max b-wave amplitude of 34 ± 19 μV occurring latently at 309 ± 113 ms ($n=6$). This supports the vision loss observed with the OKR.

3.2 | *raf*$^{-/-}$ larvae Display-Impaired Diurnal Locomotor and Visual Motor Response Behavior

Diurnal locomotor activity was measured over periods of 14 h of lights ON and 10 h of lights OFF (Figure 2A,B)

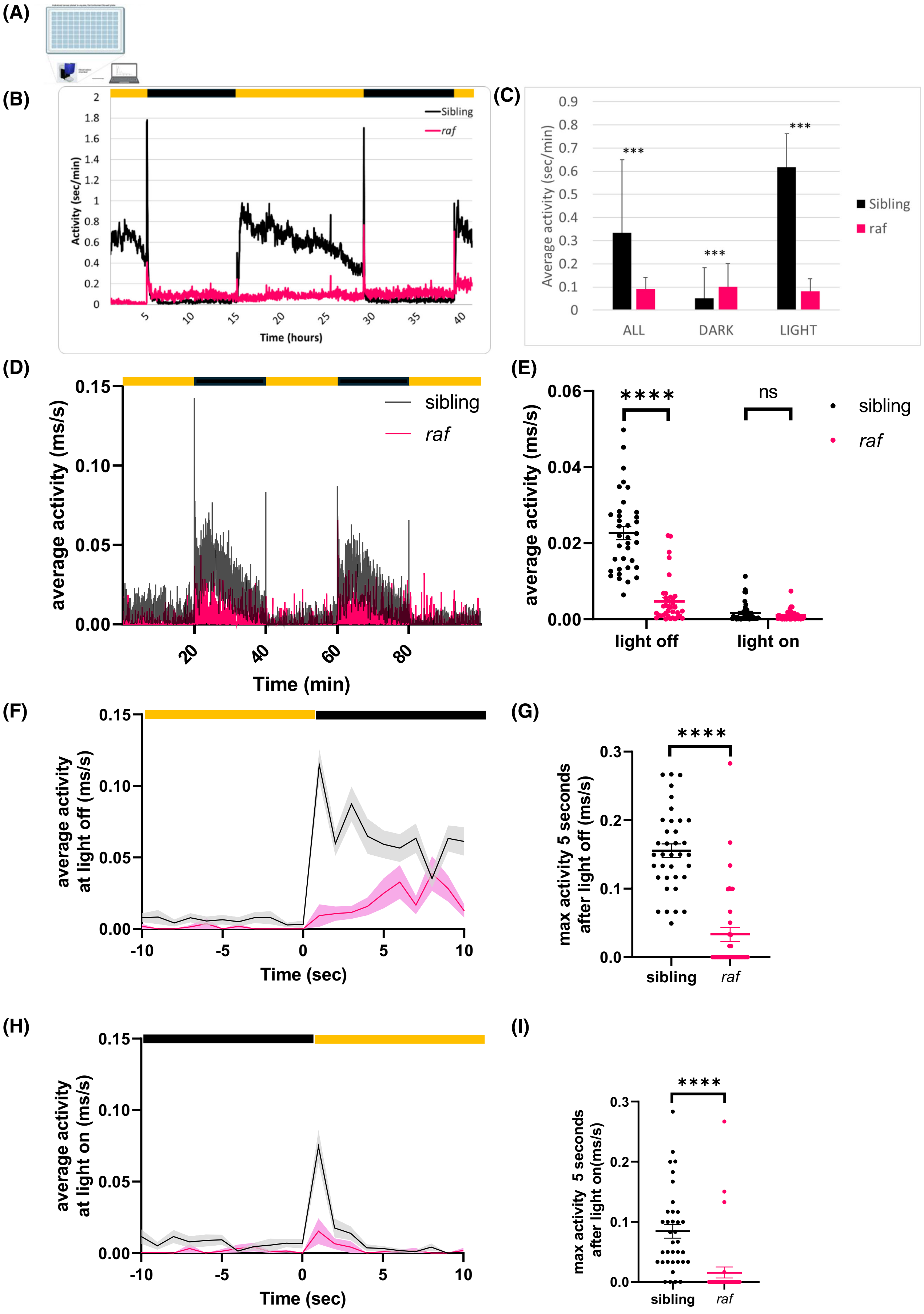
(A)
(B)
2
1.8
1.6
1.4
1.2
1
0.8
0.6
0.4
0.2
0
Activity (sec/min)
Sibling
raf
5
10
15
20
25
30
35
40
Time (hours)
(C)
0.9
0.8
0.7
0.6
0.5
0.4
0.3
0.2
0.1
0
Average activity (sec/min)
***
***
***
ALL
DARK
LIGHT
Sibling
raf
(D)
0.15
0.10
0.05
0.00
average activity (ms/s)
sibling
raf
20
40
60
80
Time (min)
(E)
0.06
0.04
0.02
0.00
average activity (ms/s)
****
ns
sibling
raf
light off
light on
(F)
0.15
0.10
0.05
0.00
average activity at light off (ms/s)
-10
-5
0
5
10
Time (sec)
(G)
0.3
0.2
0.1
0.0
max activity 5 seconds after light off (ms/s)
****
sibling
raf
(H)
0.15
0.10
0.05
0.00
average activity at light on (ms/s)
-10
-5
0
5
10
Time (sec)
(I)
0.3
0.2
0.1
0.0
max activity 5 seconds after light on(ms/s)
****
sibling
raf

from the evening of 4 dpf to the morning of 6 dpf. Whereas wild-type siblings display a pronounced increase in locomotor activity during the lights ON phase, *raf*$^{-/-}$ larvae have significantly reduced locomotor activity ($p \leq .0001$), which remained relatively constant in light ON and OFF periods (Figure 2C). However, *raf*$^{-/-}$ larvae are not immobile, they move consistently during the day, and display a noticeable burst in locomotor activity during light ON–OFF or OFF–ON changes, which is reduced compared to siblings (Figure 2C).

The visual motor response (VMR) assay was employed to quantify locomotor behavior in response to lighting changes.[18] The assay is based on bursts of activity larvae exhibit immediately following a light change and is thus indicative of photoreceptor function. The average VMR activity was significantly reduced (0.0047 ± 0.001 ms/s, $p < .0001$) in 5 dpf *raf*$^{-/-}$ larvae during the light-off period in comparison to sibling controls (0.023 ± 0.002 ms/s). During the light-on period, the average activity of the *raf*$^{-/-}$ larvae was comparable to siblings (0.0016 ± 0.0004 ms/s for siblings vs. 0.001 ± 0.0002 ms/s for *raf*$^{-/-}$) (Figure 2D,E). The activity traces at the light changes (10s before and 10s after) show that the *raf*$^{-/-}$ larvae have a reduced peak activity to lights on and off compared to siblings (Figure 2F–H). The Max-ON dot plot (max activity of individual larvae 5 s after lights ON) shows that *raf*$^{-/-}$ have reduced activity in response to the light change (0.084 ± 0.011 ms/s for siblings vs. 0.016 ± 0.009 ms/s for *raf*$^{-/-}$ $p < .0001$) (Figure 2G). The Max-OFF dot plots (maximum activity of individual larvae 5 s after lights OFF) show that *raf*$^{-/-}$ have reduced activity in response to the change to darkness (0.16 ± 0.009 ms/s for siblings vs. 0.03 ± 0.010 ms/s for *raf*$^{-/-}$, $p < .0001$) compared to sibling controls (Figure 2I). These results reveal a reduced larval response to both light onset and offset stimuli in the *raf* model, further emphasizing their impaired vision phenotype.

3.3 | *raf*$^{-/-}$ Larvae Display Defective Expression of Photoreceptor Outer Segment Markers

To assess if defects in visual behavior correlated with abnormalities in retinal cell morphology, fluorescence microscopy was performed on retinal cryosections using a panel of markers specific to various retinal cell types (Figure 3). In contrast to siblings, *raf*$^{-/-}$ retinae present with largely abolished expression of the rod photoreceptor markers 1D1 (rhodopsin) & 4C12 (unknown epitope in rods), except for in precursor cells in the peripheral ciliary marginal zone (asterisks in Figure 3B–D). In relation to cone photoreceptors, lectin PNA which labels the extracellular sheath of cone inner and outer segments[37] displayed a pattern of reduced area and intensity in *raf*$^{-/-}$ retinae (Figure 3H). Zpr-1 which labels red/green cones from the synaptic pedicle to the apex of the inner segment, but does not efficiently label the outer segment,[38] displayed a similar pattern of staining in *raf*$^{-/-}$ and siblings (Figure 3E,F). In the inner retina, PKC-alpha (bipolar), Uw-55 (Muller glia), and Sv2 (synaptic marker) labeling patterns appear equivalent in *raf*$^{-/-}$ and sibling retinae (Figure 3I–N). Preliminary data suggest that the amacrine cell marker 5e11 and ganglion cell marker zn-5 are equivalent in *raf*$^{-/-}$ and sibling eyes (*data not shown*). Overall, this analysis of *raf*$^{-/-}$ retinal markers suggests a selective defect in the staining of photoreceptor outer segment markers, with inner retina markers largely unaffected.

3.4 | *raf*$^{-/-}$ larvae display pronounced defects in outer segment morphogenesis

To further elucidate the underlying etiology of visual impairment in the *raf*$^{-/-}$ zebrafish, retinal cell structure was analyzed by light microscopy (LM). *raf*$^{-/-}$ larvae raised on a standard light: dark cycle were fixed at

FIGURE 2 *raf* zebrafish have visual motor response defects. (A) Schematic representation of the visual motor response (VMR) assay. Larvae are individually plated in wells in a square-bottom 96-well plate before placement in the observation chamber. (B) The normal activity (average seconds activity per minute) of *raf* mutants (magenta line) and their wild-type siblings (black line) was recorded over 42 h, using the Viewpoint system, from the evening of 4 dpf (6.30 pm) to the morning of 6 dpf (10.30 am). The black bars represent two 10-h night periods. (C) Average activity levels over the entire experiment (all), during the night time (dark) and during the day time (light). Magenta bar = average activity of 55 *raf* mutants; black bar = average activity of 80 wild type (wt) siblings. Student's *t*-test, where ***$p \leq .0001$ (D) Visual motor response (VMR) activity traces displaying the average activity of sibling (black) and *raf* mutants (pink) across the entire 100-min experimental paradigm. (E) Dot plot of the average activity of each fish over the combined 40-min light-off period and 40-min light-on period. Mann–Whitney test; $p < .0001$ for light off, ns$p = .7859$ for light on. (F and H) Activity traces displaying the average activity of the larvae 10 s before and after the light turned off (F) or turned on (H). The average is represented by the line and the SEM shown by the shaded gray or pink. (G and I) Dot plots of the max activity of each fish within 5 s of the light off (G) or light on (I). Mann–Whitney test: ****$p < .0001$. Yellow and black bars represent 20-min periods of lights on and off, respectively. $N = 3$ independent biological replicates with $n = 12$ larvae per replicate. Error bars are the mean ± SEM.

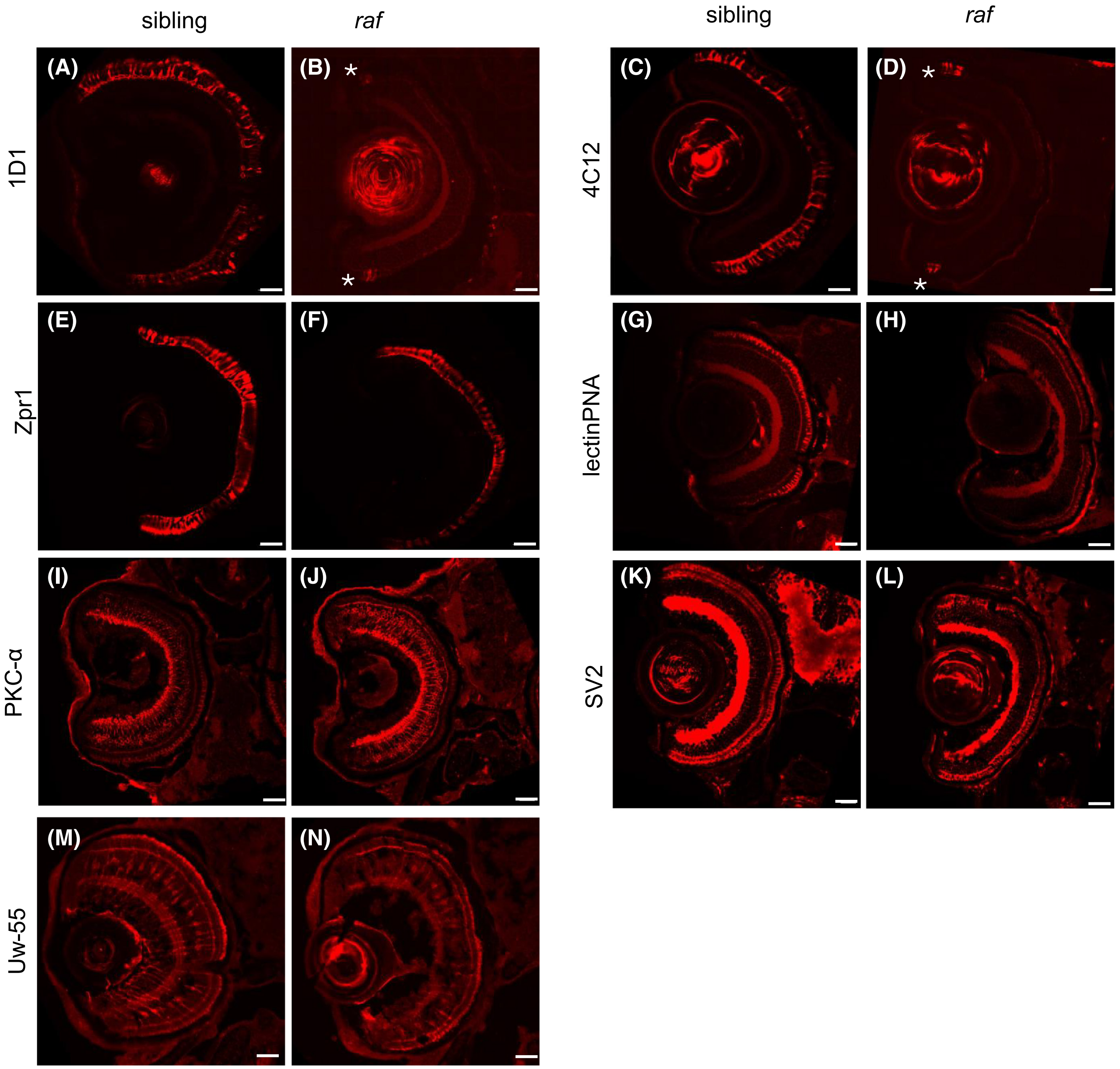

FIGURE 3 *raf* zebrafish have reduced outer retinal markers but inner retinal markers are not changed. (A–N): Images of retinal cross sections from wild-type siblings (A, C, E, G, I, K, and M) and *raf*$^{-/-}$ (B, D, F, H, J, L, and N) stained with antibodies to retinal cell populations (red); 1D1 (A and B), 4C12 (C and D), Zpr1 (E and F), lectin PNA (G and H), PKC-α (I and J), SV2 (K and L), and Uw-55 (M and N). Asterisks show faint 1D1/4C12 staining in the peripheral retina in *raf*$^{-/-}$ mutant images. Sections were generated with cryostat and imaged with a confocal microscope with 40x objective (A–N). Larvae were 6 dpf (A-L) and 4 dpf (M and N). Scale bar = 20 μm (A–N).

131 hpf for 48 h prior to embedding, sectioning, and imaging. LM images reveal *raf*$^{-/-}$ larvae possess a thinner photoreceptor layer with vacuole-like structures in the photoreceptor and RPE layers, plus large gaps between the lens and inner peripheral retina and between the lens and the cornea (Figure 4A,B). Morphometric analysis of central retinal lamination revealed that the *raf*$^{-/-}$ inner plexiform layer was reduced by 14% (13.3 ± 0.35 μm vs. 11.5 ± 0.3 μm for siblings vs. *raf*$^{-/-}$, $p = .0211$) and the *raf*$^{-/-}$ photoreceptor layer reduced by 44% (10.6 ± 0.56 μm vs. 5.9 ± 0.82 μm for siblings vs. *raf*$^{-/-}$, $p = .009$) (Figure 4C). No significant differences were observed for the diameter of the *raf* lens, the inner nuclear layer, the outer plexiform layer, the ganglion cell layer, or the RPE layer thickness (Figure 4C). Moreover, the interdigitation of RPE cells between the photoreceptor's outer segments in wild-type siblings is not visible in *raf*$^{-/-}$ mutants (Figure 4A′,B′). Vacuole-like structures present within *raf*$^{-/-}$ RPE cells and at the boundary of the outer nuclear layer and photoreceptor outer

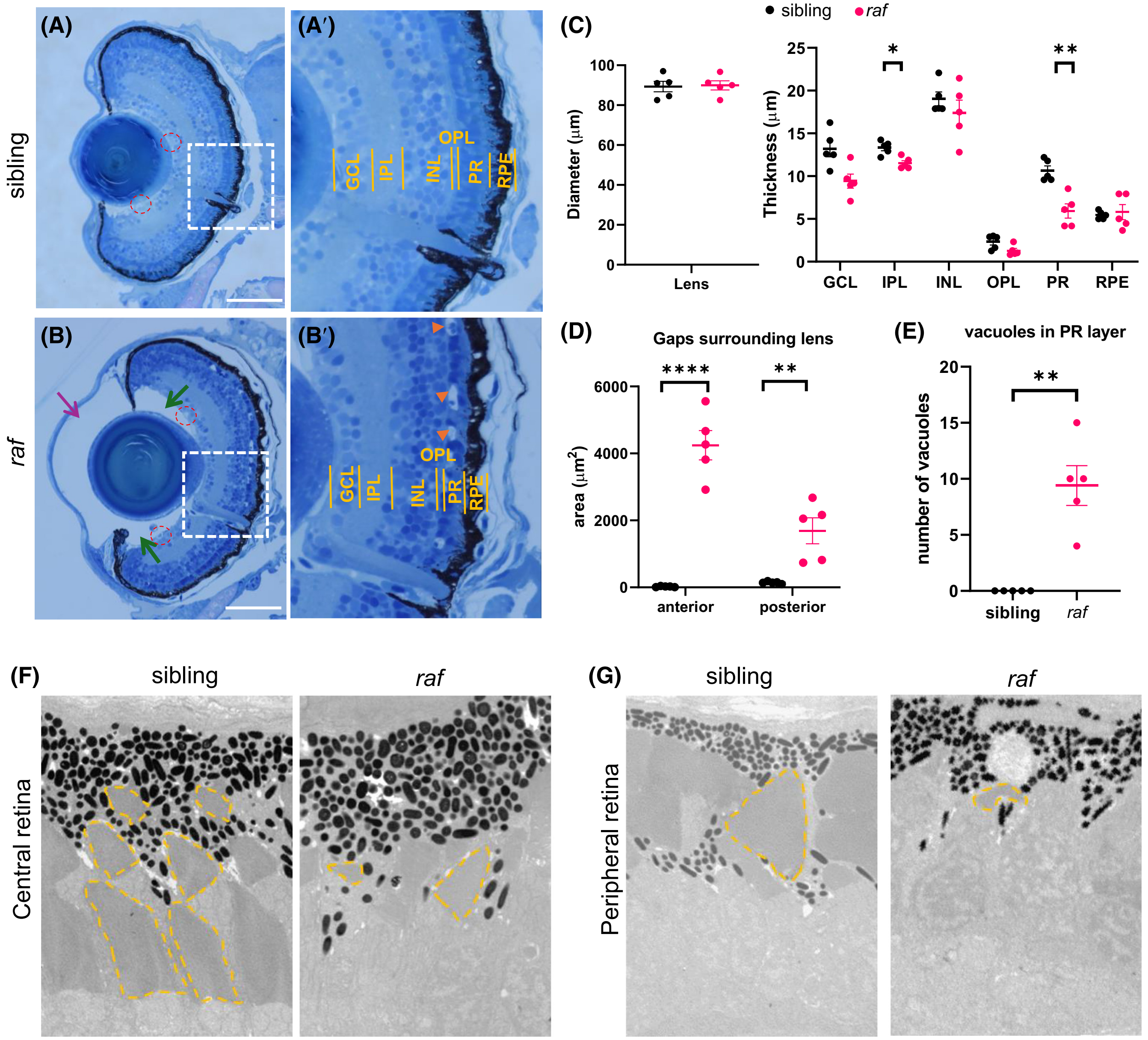

FIGURE 4 Histology and morphometric analysis of *raf*$^{-/-}$ eyes reveal a range of ocular and retinal layer defects. (A and B) Representative retinal cross sections stained with toluidine blue of sibling (A and A′) and *raf*$^{-/-}$ (B and B′). Sections were generated using an ultramicrotome and imaged with a 40x objective using a light microscope. (A′ and B′) shows the area from the white box in A-B with the different retinal layers labeled (A′ and B′). GCL, ganglion cell layer; IPL, inner plexiform layer; INL, inner nuclear layer; OPL, outer plexiform layer; PR, photoreceptor; RPE, retinal pigment epithelium. In A and B, red dashed circles surround single hyaloid vessels. In B, the purple arrow points to the gap anterior to the lens, and the green arrows point to the gap posterior to the lens. In A″ and B″ the vacuoles are marked with orange arrows. Scale bar = 50 μm. (C) Dot plots show the thickness of the lens and retinal cell layers. Unpaired *t*-test corrected for multiple comparisons with Bonferroni–Dunn method. IPL: **p* = .0211, PR: ***p* = .0090. Data are mean ± SEM. (D) Dot plot shows the area of gaps around the lens. Unpaired *t*-test, *****p* < .0001, ***p* = .004. (E) Dot plot shows the total number of vacuoles in the PR layer observed in each section. Data is mean ± SEM. *n* = 5 larvae per genotype. Morphometric analyses were performed using Image J. (F and G) Representative transmission electron micrographs from retinal cross sections from siblings and *raf*$^{-/-}$ at 6 dpf. Both central (F) and peripheral (G) regions of the retina are shown. Yellow dotted line marks the outline of outer segments.

segment layer were never observed (0 vs. 9.4 ± 3.975 vacuoles for siblings vs. *raf*$^{-/-}$) (Figure 4E) in siblings (orange arrows Figure 4B′). In *raf*$^{-/-}$ larvae, large gaps were present between the lens and retina, and lens and cornea (arrows Figure 4B). These gaps are significantly increased in *raf*$^{-/-}$, both anterior to the lens (23.54 μm^2 vs. 4245 μm^2 for siblings vs. *raf*$^{-/-}$; *p* < .0001, purple arrow) and posterior to the lens (142.9 μm^2 vs. 1690 μm^2 for sibling vs. *raf*$^{-/-}$; *p* = .003, green arrows) (Figure 4D). Interestingly, hyaloid vessels (red dashed circles in

Figure 4A,B) which should still be tightly attached to the lens at this early developmental stage, as observed in wild-type siblings, lack normal attachment to the inner retina in *raf*$^{-/-}$ larvae.

Electron microscopy revealed that, *raf*$^{-/-}$ have sparse, small photoreceptor outer segments in the peripheral and central retina, with a more severe phenotype observed in the peripheral outer segments (Figure 4F,G). In comparison, the wild-type siblings have multiple large outer segments in the peripheral and central retina (outlined in orange dashed line), with typical basal to apical orientation.

3.5 | *raf*$^{-/-}$ results from a nonsense point mutation in the *emc1* gene

To initially map the *raf* mutation, bulked segregant analysis was performed as previously described using microsatellite-based primer pairs evenly distributed across the zebrafish genome.[39] Using this strategy, marker z4003 was found to cosegregate with *raf*, placing the gene on linkage group 23 (*data not shown*). Identification of the *raf* gene was achieved using a combination of RNA sequencing (RNAseq), and whole genome sequencing (WGS) (Figure 5A–C). Positional cloning and mutation mapping of the RNAseq and WGS data using the MMAPPR pipeline[34] or a custom algorithm[23] linked the *raf* mutation to chromosome 23, within base position 20–30 MB (Figure 5A–C). Combining the DNA and RNA sequencing results, a table of candidate *raf* genes was generated (Figure 5D). Noticeably, a paralog of the human *EMC1* gene previously linked to visual impairment[14,15] scored highly and contained a point mutation resulting in an early stop codon in *raf*$^{-/-}$. Sanger sequencing confirmed that *raf*$^{-/-}$ was homozygous for a single nucleotide mutation in exon 4, at position 117, in the *emc1* gene (Figure 5E). This results in the wild-type TTG codon for leucine being mutated to TAG generating an early STOP codon (Figure 5E). The zebrafish protein has 68% identity to the human EMC1 and the mutated leucine in *raf*$^{-/-}$ is evolutionarily conserved in both species (Figure 5F). Structural modeling predicts zebrafish Emc1 contains transmembrane domains similar to the human EMC1 protein[40,41] and has two beta-propellers (green sheets in Figure 5G) that sit within the ER lumen (Figure 5G). Modeling of the human protein found that this lumenal domain interacts with the EMC7 and EMC10 subunits and is necessary for the functioning of the entire complex.[42] The majority of disease mutations in humans (marked in green in Figure 5F) are present in the lumenal domain of EMC1 highlighting its crucial role. In *raf*$^{-/-}$, Emc1 is truncated to the first 116 amino acids, therefore, 87% of the protein is missing with the majority of the lumen and transmembrane domains lost (Figure 5G). In agreement, when *emc1* transcript levels were quantified by qPCR, levels in *raf*$^{-/-}$ were significantly ($p = .0056$) reduced (45%) compared to wild-type siblings (Figure 5H) suggesting nonsense-mediated decay. Mutations in *emc3*, another member of the EMC complex, display decreased OKR under red light in the zebrafish partial optokinetic response b (*pob*) mutant.[43] Notably, unlike *emc1*, *emc3* levels are unaffected in *raf*$^{-/-}$ (Figure 5H). The expression of *emc1* was queried using online tools from previously published sc-RNAseq data from the adult retina[44] and was found to display a low mean expression (0.094–0.213) across all cell types (Figure 5I). *emc1* did not display cell-specific expression as compared to known rod and cone genes, for example, *grk1a* and *grk7a* (Figure 5I). With the identification of the responsible gene, the *raf* zebrafish is subsequently called *emc1*$^{-/-}$.

FIGURE 5 *emc1* was identified as the gene mutated in *raf*$^{-/-}$ zebrafish. (A) Traces of sibling (peach) and *raf*$^{-/-}$ (blue) for each chromosome from whole genome sequencing. Purple box highlights chromosome 23. (B) Trace showing the positions along chromosome 23. (C) *raf*$^{-/-}$ mutation mapping from RNA sequencing. Graphs depict the Euclidean distance scores raised to sixth power across the genome and across chromosome 23. The vertical gray lines delineate chromosome edges and chromosome widths represent the relative number of SNPs on the chromosome. Loess fit curve was calculated using the data. (D) Table showing *raf*$^{-/-}$ gene candidates and types of mutations observed. (E) Sanger sequencing traces from wild-type siblings, heterozygous siblings, and homozygous *raf*$^{-/-}$mutants. Black box highlights the leucine codon that is mutated to become a stop codon due to the single nucleotide change. Heterozygous animals can be identified by the presence of the double AT peak (*N*). (F) Multiple sequence alignment of human EMC1 compared with zebrafish Emc1. Alignment was generated using ClustalW. Colors represent percentage identity and were annotated using Jalview. The mutation point in *raf*$^{-/-}$is marked by purple. (G) The predicted 3D structures of zebrafish wild type and mutant Emc1 were generated with Swiss Model software (https://swissmodel.expasy.org/) using A0A671TKS0.1.A as a template. Left-Colors represent secondary structures with beta sheets (green) and alpha helices (purple). Gray marks the predicted transmembrane portion. The right colors represent the different proteins wild-type Emc1 (cyan) and *raf* Emc1 (gold). (H) *emc1* and *emc3* transcript expression levels in *raf*$^{-/-}$mutants measured by qPCR from pooled RNA extracted from whole zebrafish larvae at 5 dpf. Levels were normalized by β-actin expression. Red line is the level of expression of siblings. Three replicates of 20 larvae. Unpaired *t*-test, $^{**}p = .0056$, ns$p = .11$. (I) Expression of *emc1* in the zebrafish retina from online scRNA-seq data https://proteinpaint.stjude.org/F/2019.retina.scRNA.html. Red marks cells with *emc1* expression. Heat map displays the mean expression of *emc1, grk1a, and grk7a* in each cell type.

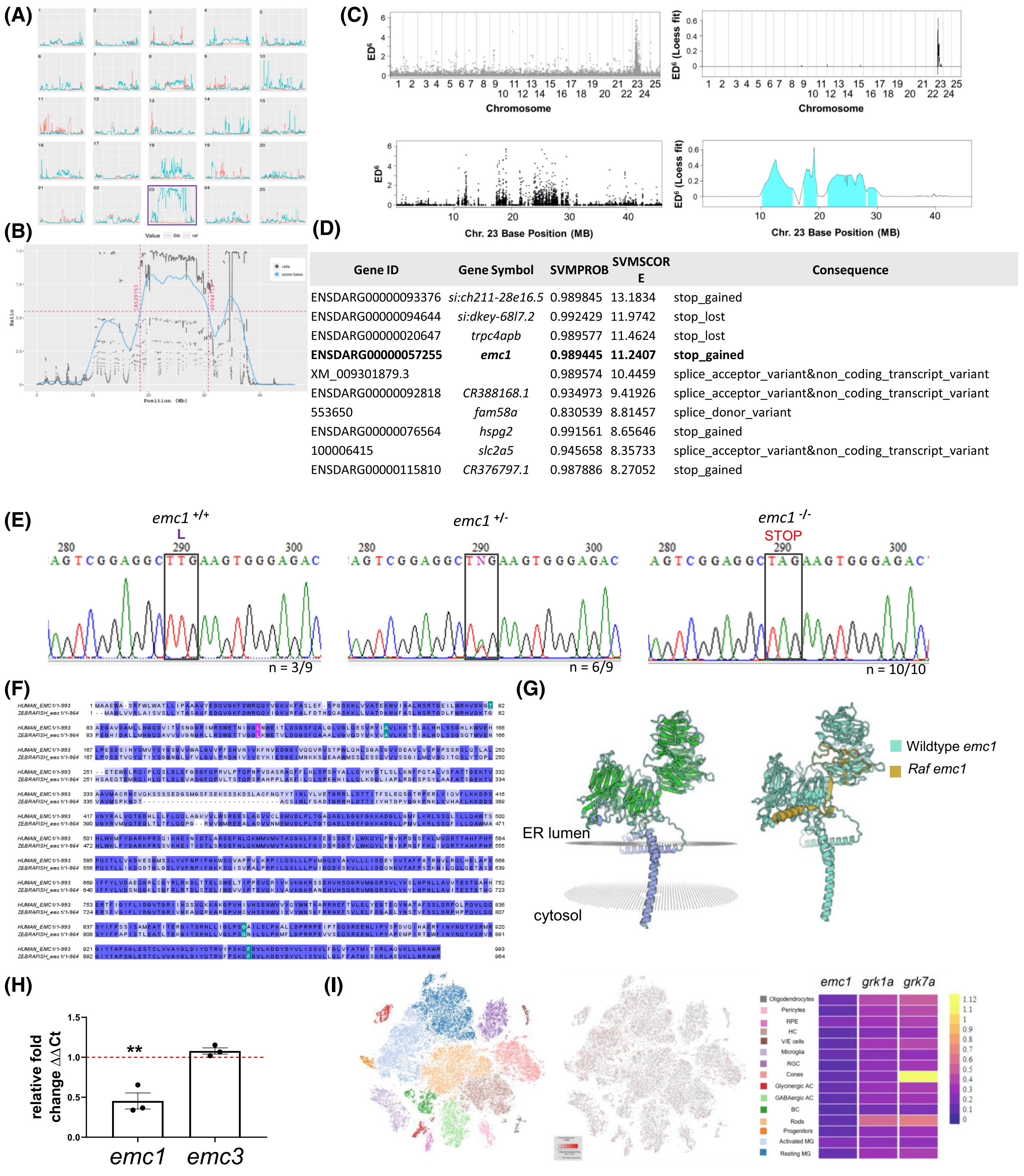

Gene ID	Gene Symbol	SVMPROB	SVMSCORE	Consequence
ENSDARG00000093376	*si:ch211-28e16.5*	0.989845	13.1834	stop_gained
ENSDARG00000094644	*si:dkey-68l7.2*	0.992429	11.9742	stop_lost
ENSDARG00000020647	*trpc4apb*	0.989577	11.4624	stop_lost
ENSDARG00000057255	***emc1***	**0.989445**	**11.2407**	**stop_gained**
XM_009301879.3		0.989574	10.4459	splice_acceptor_variant&non_coding_transcript_variant
ENSDARG00000092818	*CR388168.1*	0.934973	9.41926	splice_acceptor_variant&non_coding_transcript_variant
553650	*fam58a*	0.830539	8.81457	splice_donor_variant
ENSDARG00000076564	*hspg2*	0.991561	8.65646	stop_gained
100006415	*slc2a5*	0.945658	8.35733	splice_acceptor_variant&non_coding_transcript_variant
ENSDARG00000115810	*CR376797.1*	0.987886	8.27052	stop_gained

3.6 | Loss of *emc1* is linked to defective zebrafish ocular vasculature

A recent report linked loss of *Emc1* function in mice to retinal vasculature defects.[45] This finding, combined with the previously observed abnormality in hyaloid vessels in LM sections (Figure 4B), led us to investigate the impact of the *emc1* mutation on developing zebrafish hyaloid vessels. Heterozygous *emc1*$^{+/-}$ adults were incrossed into the *Tg(fli1:EGFP)* transgenic line, in which the promoter for the endothelial marker *fli1* drives the EGFP expression in all blood vessels.[46] Morphological analysis of the hyaloid vasculature (HV) surrounding the lens, in addition to the intersegmental vessels (ISV) in the trunk was carried out in *raf*$^{-/-}$;*Tg(fli1:EGFP)*. At 72 hpf, there is no apparent abnormality in the trunk ISV formation of *emc1*$^{-/-}$ larvae in comparison to sibling controls (Figure 6A,B). The HV develops in zebrafish from 24 to 72 h following fertilization, and at 5 dpf, it consists of four to five main branches tightly attached to the lens, radiating from the hyaloid artery at the optic disc toward the anterior, avascular part of the lens. These vessels branch out via angiogenesis, forming a characteristic hyaloid vasculature pattern that extends to the annular vein surrounding the anterior part of the crystalline lens.[47] In *emc1*$^{-/-}$ larvae, abnormal HV development was observed at 5 dpf (Figure 6C,D). While in sibling controls, fluorescent imaging of the GFP positive vessels shows that the HV is tightly attached to the lens, forming the typical well-defined "basket" structure surrounding it (Figure 6C). In comparison, *emc1*$^{-/-}$ eyes exhibit abnormal HV which is disorganized and detached from the lens (Figure 6D), consistent with the abnormalities observed in the LM sections.

3.7 | Loss of *emc1* in *raf*$^{-/-}$ is linked to defective expression and localization of photoreceptor OS proteins

Previous reports state EMC is responsible for the quality control of membrane proteins[48] and the biogenesis of multipass membrane proteins[11,49] and a subset of GPCRs.[13] In mouse and fly photoreceptors, Emc1 is required for the synthesis of rhodopsin and outer segment proteins, and is linked to progressive retinal degeneration.[10,50] Therefore, the expression and localization of membrane-associated and cytoplasmic proteins in *emc1*$^{-/-}$ zebrafish photoreceptors were investigated by immunohistochemistry and reporter-tagged proteins (Figure 7).

The *emc1*$^{-/-}$ line was crossed into the *Tg(gnat2:rab28-eGFP)* reporter line that displays enriched GFP fluorescence in cone outer segments.[51] Notably, Rab28 is reported as a farnesylated ciliary G-protein.[52] Confocal imaging of retinal photoreceptors revealed *emc1*$^{-/-}$ zebrafish present with significantly ($p < .0001$) reduced GFP-tagged Rab28 expression levels in the photoreceptor outer segment region (Figure 7A,B). Rab28 is expressed in *emc1*$^{-/-}$ zebrafish but does not display the same localization pattern as wild-type siblings. In *emc1*$^{-/-}$, rab28 localizes throughout the photoreceptor and is observed apical of the nucleus down to the synaptic terminal. In comparison, the cone OS displays strong GFP fluorescence in siblings (Figure 7A–C,F,H,J). When quantified across cone photoreceptors, *emc1*$^{-/-}$ larvae have significantly reduced Rab28-GFP fluorescence intensity (area under the curve of 213.1 ± 12.96) compared to siblings (area under the curve of 570.9 ± 28.38) (Figure 7C,D).

Peripherin 2 (Prph2), a member of the transmembrane 4 or tetraspanin superfamily, is involved in outer segment morphogenesis and renewal.[53] In wild-type zebrafish, Prph2 is more highly expressed in cone outer segments than rod outer segments.[54] In 5 dpf siblings, Prph2 selectively labeled the membrane of the cone outer segment and overlapped with the rab28-eGFP signal (Figure 7E,E′). The expression levels of Prph2 are dramatically reduced in *emc1*$^{-/-}$ larvae and appear to label regions of the photoreceptor largely distinct from the rab28-eGFP signal, which is likely due to the small outer segment present in *emc1*$^{-/-}$ as seen by electron microscopy (Figure 7F′).

The G Protein Subunit Beta 3 (GNB3) is one of the subunits of cone transducin and plays a role in phototransduction.[55,56] The subunit is a WD repeat G protein and associates with 7 transmembrane receptors and the membrane-anchored alpha and gamma subunits. Gnb3 extensively labels the inner and outer segments in siblings at 5 dpf (Figure 7G,G′). In *emc1*$^{-/-}$, Gnb3 levels are drastically reduced but can still be observed around the cell body of the cone cells (Figure 7H,H′).

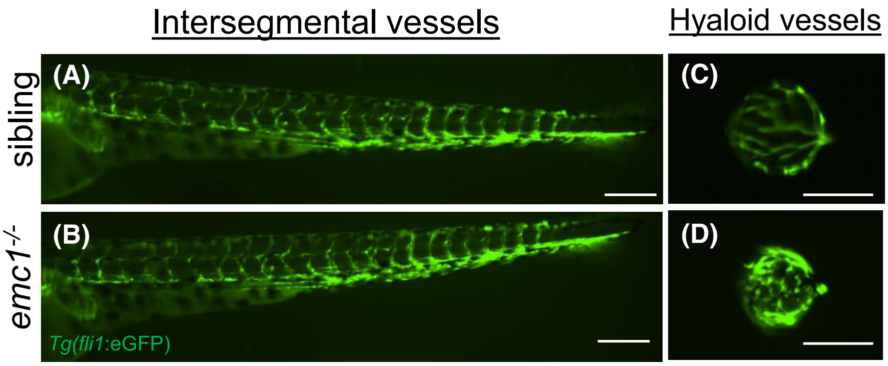

FIGURE 6 Hyaloid vessels are dysregulated in *emc1*$^{-/-}$ zebrafish. (A and B): Fluorescent images displaying lateral views of the trunk of wild-type sibling (A) and *emc1*$^{-/-}$ (B) larvae at 5 dpf carrying the *Tg(fli1:GFP)* transgene (green). Scale bar is 200 μm. (C and D): Fluorescent images displaying lateral views of dissected lenses from wild-type siblings (C) and *emc1*$^{-/-}$ (D) larvae at 5 dpf carrying the *Tg(fli1:GFP)* transgene (green) to image the hyaloid vessels. Scale bar is 50 μm.

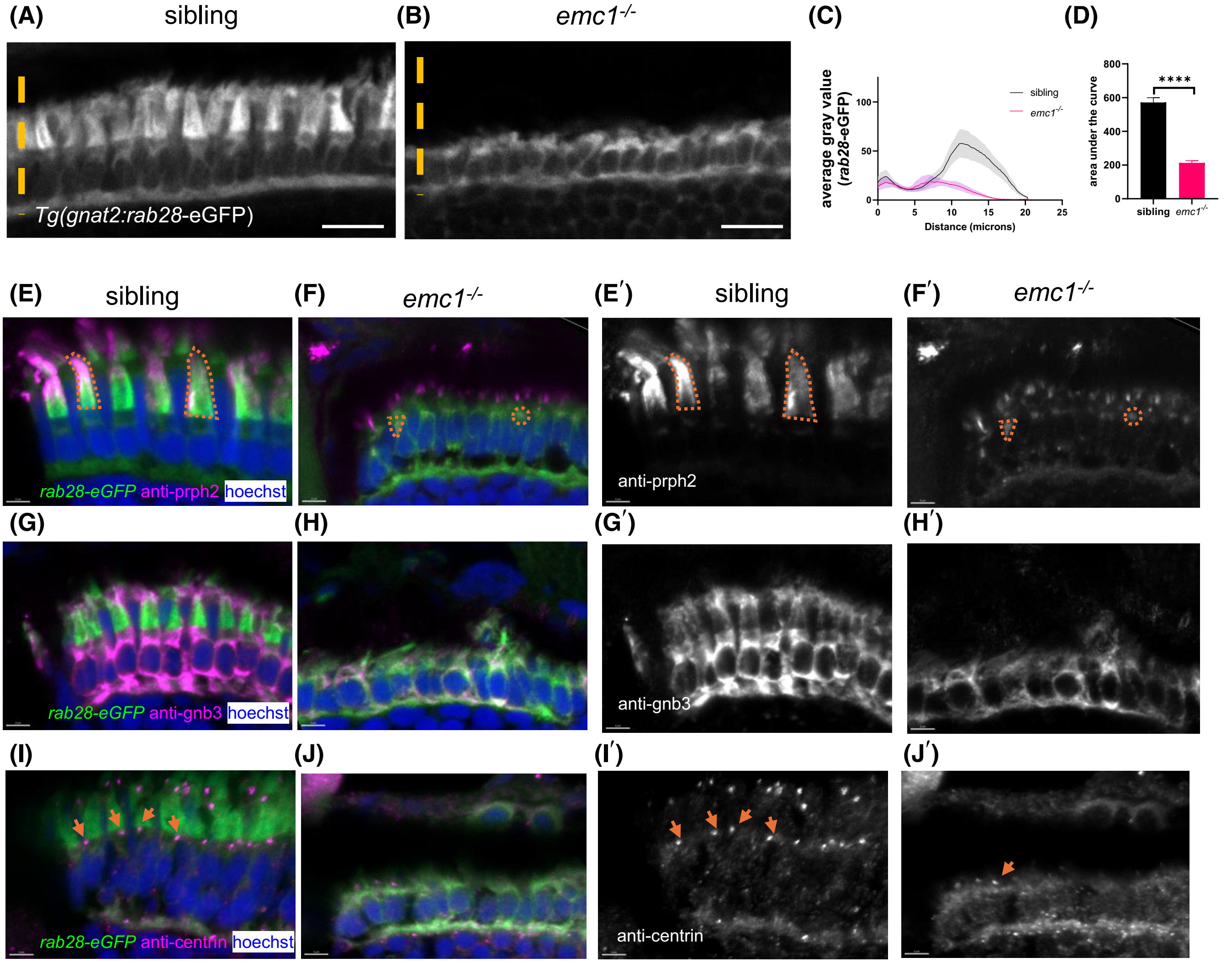

FIGURE 7 *Emc1*$^{-/-}$ display defective expression and localization of outer segment proteins. (A and B) Retinal cross sections of *Tg(gnat2:Rab28-eGFP)* transgenic larvae. Orange line represents how the gray value was measured. (C) Graph shows the average gray value of the GFP fluorescence of sibling (black) and *emc1*$^{-/-}$ (pink) along the line. Data is mean ± SEM. 10 cells per larvae were measured. Three replicates of 9–10 larvae per genotype. (D) Box plot shows the area under the curve of the average gray value. Unpaired *t*-test, ****$p < .0001$. (E–J) Retinal cross sections of siblings and *emc1*$^{-/-}$ carrying the transgene *Tg(gnat2:Rab28-eGFP)* (green) labeled with anti-Prph2 (E and F), anti-Gnb3(G and H), anti-centrin (I and J) (magenta), and Hoechst (blue). (E′–J′) Shows E and J images with the anti-Prph2, Gnb3, and centrin labeling only (white). In E–F′ orange marks the region covered by the Prph2 labeling in two cells. In I–J′ orange arrows point to the centrin labeled puncta. Scale bar = 10 μm (A) and 4 μm (E–J′).

Centrin is a connecting cilium protein that labels the junction between the inner segment and outer segment.[57] It is a member of the EF-hand superfamily of calcium-binding proteins and part of the centrosome. In 5 dpf siblings, centrin staining appears as puncta at the apical side of the cone cell body just below the outer segment (orange arrows in Figure 7I,I′). In contrast, the *emc1*$^{-/-}$ have fewer centrin-positive puncta, and the rab28-eGFP signal is largely basal to centrin, unlike in siblings where the rab28-eGFP signal is apical to centrin (Figure 7I,I′,J,J′). Overall this suggests the loss of *emc1* in zebrafish leads to changes in localization and abundance of many types of membrane-associated proteins within the cone photoreceptors.

3.8 | RNAseq reveals dysregulated expression of phototransduction genes in *emc1*$^{-/-}$

RNAseq data from 5 dpf wild type siblings and *raf*$^{-/-}$ zebrafish eyes was comprehensively analyzed to identify transcripts significantly altered due to loss of *emc1* expression. A total of 24 286 genes were quantified in the samples and transcript expressions were filtered for genes with statistically significant adjusted p value ≤.05 and log2 fold change value of 1 and or −1. These stringency cutoffs revealed 321 transcripts significantly upregulated and 409 transcripts significantly downregulated in *raf*$^{-/-}$ compared to siblings (Figure 8B). The upregulated and downregulated gene lists were processed for pathway enrichment analysis using DAVID and Shinygo (Figure 8E,F). The top KEGG pathways that were annotated/mapped in the upregulated genes were "*protein processing in endoplasmic reticulum*" (25 genes, 8.3%) and "*aminoacyl tRNA biosynthesis*" (13 genes, 4.3%). The down-regulated genes mapped to the KEGG pathways "*phototransduction*" (37 genes, 9.9%) and "*neuroactive ligand receptor interaction*" (16 genes, 4.3%). Quantitative PCR was run using total RNA extracted from whole 5 dpf siblings or *emc1*$^{-/-}$ zebrafish, targeting 4 transcripts upregulated or downregulated from the gene lists to validate the data (Figure 8C,D). Two of the upregulated genes (*irg1l, fosl1a*) in *emc1*$^{-/-}$ displayed a significant increase compared to siblings (*irg1l*: 11.294 ± 3.142, *fosl1a*: 1.998 ± 0.154) while the other two genes (*isg15, fga*) showed positively increasing trends (*isg15*: 3.227 ± 1.366, *fga*: 1.692 ± 0.286). Expression of all 4 selected down-regulated genes was validated to have a significantly decreased expression in *emc1*$^{-/-}$ compared to siblings (*rhol*: 0.204 ± 0.066, *pth1b*: 0.270 ± 0.057, *pde6ga*: 0.295 ± 0.125, *gnat1*: 0.215 ± 0.094).

4 | DISCUSSION

In this study, we present original findings on the zebrafish *emc1*$^{-/-}$ knockout as a novel model of inherited retinal dystrophy. *emc1*$^{-/-}$ larvae display severe visual behavior and retinal function impairments, abnormal anterior and posterior ocular morphology, and acute defects in photoreceptor outer segment morphogenesis. This represents the first vertebrate model of global germline loss of Emc1 function and through characterizing its phenotypic traits, we elucidate the fundamental role of this protein in retinal homeostasis and vision.

Originally identified as the *raf* mutant from a forward genetic screen, endoplasmic reticulum complex subunit 1 (*emc1*) was identified as the causative gene by whole genome and transcriptome sequencing coupled with positional mapping. Vertebrate *Emc1* genes encode the largest subunit of the endoplasmic reticulum complex (EMC) which together with 9 other proteins are reported regulating the synthesis, stabilization, and/or trafficking of membrane proteins including rhodopsin, Na^+/K^+ ATPase, and acetylcholine receptors.[9,10] EMC1 is evolutionary conserved and protein sequences show high percent protein identity in *Drosophila (31%), C. elegans (38%), Mus musculus (93%), and Danio rerio (68%)* compared to human EMC1 (https://www.uniprot.org/). Genetic studies reveal mutations in *EMC1* associated with human disease. Homozygous variants in *EMC1* that generate missense or premature stop codons are reported in patients with retinitis pigmentosa,[14] global developmental delay, autism spectrum, visual impairment, and cerebellar atrophy.[15,16,58] All have been classed in ClinVar as pathogenic or likely pathogenic. *EMC1* heterozygous variants were identified in 2 individuals with familial exudative vitreoretinopathy (FEVR)[45] and trio exome sequencing studies of congenital heart disease patients.[59,60] However, experimental proof demonstrating the pathogenicity of these heterozygous variants is absent. The cellular and molecular basis for the human disease phenotypes due to *EMC1* dysfunction is not clear, demonstrating a need for relevant in vivo animal models, and phenotypic characterization. As such, the zebrafish *emc1*$^{-/-}$ mutant provides a unique model to understand the role of Emc1 in biology and disease.

In zebrafish, the loss of *emc1* causes rapid retinal dysfunction by 5 dpf and homozygous animals do not survive past 8/9 dpf (*data not shown*), presumably due to an inability to feed but potentially linked to non-ocular roles of *emc1*. While *emc1* expression is not considered spatially restricted in zebrafish, the larval knockout phenotypes seem to be selective to the retina and vision, as the gross morphology of *emc1*$^{-/-}$ fish is not affected by 5 dpf, apart from

FIGURE 8 RNA sequencing in *emc1*$^{-/-}$ eyes reveals that the expression of phototransduction genes is reduced. (A) Schematic of RNA sequencing workflow. Total of 40 larvae per sample/genotype: 80 eyes per sample/tube. RNA sequencing was performed in NEI/NIH on Illumina 2500 and analyzed with RNAlysis. Pathway analysis was performed with ShinyGo/DAVID. (B) Volcano plot displaying the genes that are differentially expressed; downregulated (blue) and upregulated (red) in *raf* versus siblings. (C and D) Expression levels of selected downregulated (C) and upregulated (D) genes measured by qPCR in *emc1*$^{-/-}$ compared to siblings from pooled RNA extracted from whole zebrafish larvae. Levels were normalized by β-actin expression. Black line represents the expression of the sibling. Data are mean ± SEM. Three replicates of 20 larvae. Unpaired *t*-test, $^*p < .05$, $^{**}p < .01$, $^{***}p < .001$. Tables show the genes from the downregulated/ upregulated gene list with the calculated log 2-fold change from the RNA seq compared to values from the qPCR. (E and F) Bar graphs show the top KEGG Pathways associated with the downregulated (E) and upregulated (F) genes. The number of genes that were mapped to each pathway is shown. (G and H) Bar graphs show the transcripts identified by RNAseq (log fold change <−1 or >1) for phototransduction (G) and protein processing in the endoplasmic reticulum (H). Genes are color-coded to group different cell types or parts of the pathway.

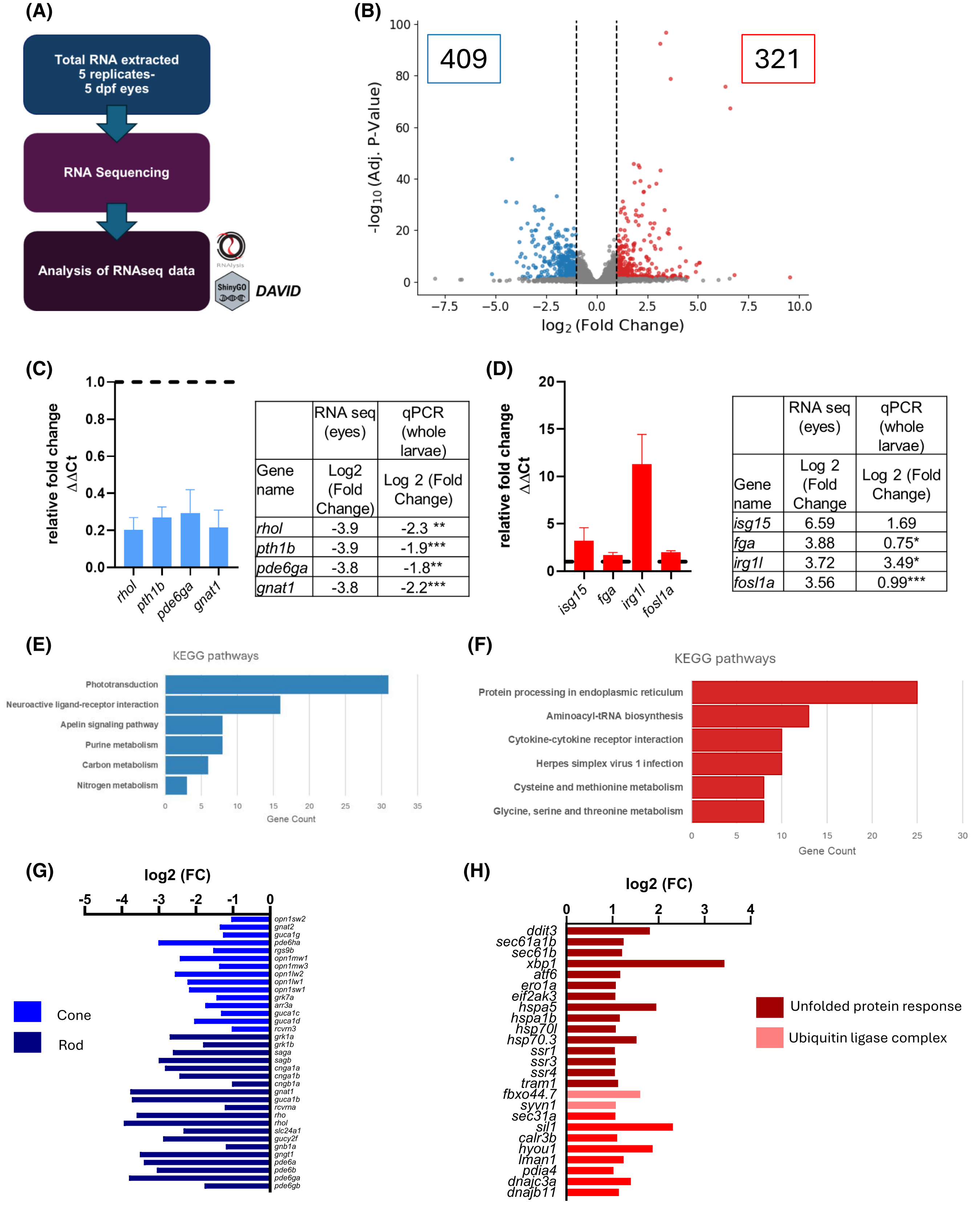

	RNA seq (eyes)	qPCR (whole larvae)
Gene name	Log2 (Fold Change)	Log 2 (Fold Change)
rhol	-3.9	-2.3 **
pth1b	-3.9	-1.9***
pde6ga	-3.8	-1.8**
gnat1	-3.8	-2.2***

	RNA seq (eyes)	qPCR (whole larvae)
Gene name	Log 2 (Fold Change	Log 2 (Fold Change)
isg15	6.59	1.69
fga	3.88	0.75*
irg1l	3.72	3.49*
fosl1a	3.56	0.99***

a deflated swim bladder (a common occurrence in blind zebrafish larvae). This contrasts with other EMC1 models in which global loss of EMC1 causes a range of profound developmental defects. In *Drosophila*, homozygotes of the *EMC1*^{655G} null allele are pupal lethal.[10,16] Pupal lethality of over 80% is also observed when the expression of RNAi targeting fly *EMC1* was induced either ubiquitously or only in glial cells. In the glia-specific knockdown, the 15% of flies that develop display climbing defects and eventually die by day 15. Expression of the same RNAi only in neurons did not lead to lethality. In *C.elegans* when *emc-1* is targeted by RNAi, embryonic lethality was not observed but the worms displayed developmental arrest and incoordination.[9] In *Xenopus*, when *emc1* was knocked down using morpholino oligonucleotides the tadpoles displayed abnormal pigment, reduced diameter of the outflow tract, loss of craniofacial cartilage, and reduced motility.[61] A global *Emc1* knockout in a rodent model has not been reported. Cell-specific knockouts of *Emc1* in murine photoreceptors or endothelial cells have been published which display progressive retinal degeneration and deficient retinal vessel development.[45,50] Other EMC subunits are linked to retinal degeneration such as Emc3[43,62–64] and Emc6.[63,65] In the zebrafish *emc1*$^{-/-}$ knockout, transcript expression of all the other subunits including *emc3* and *emc6* (data not shown) is not significantly changed. With the establishment of the zebrafish *emc1* knockout model, new research opportunities arise to investigate the potential effects of *emc1* variants in non-ocular tissues, including variants that have been linked to human patients but have yet to be experimentally confirmed. Therefore, the zebrafish global *emc1*$^{-/-}$ knockout provides a different, relevant model to understand EMC-related human disease.

EMC1 is linked to visual dysfunction. Patients carrying *EMC1* variants present with visual impairment, abnormal visual evoked potentials, and abnormal ERGs.[15] In the cell-specific knockout of *Emc1* in rod photoreceptors, the scotopic ERG amplitude of both a-wave and b-wave was reduced by ~50%.[50] Here, the dark-adapted a-wave amplitude was reduced by nearly 50% and the b-wave amplitude by ~85%. At this developmental stage, vision is predominately cone-mediated as rod photoreceptors are not fully developed or functional until 12–15 dpf.[66–68] In addition, the latency of both a-wave and b-wave peaks was delayed compared to their siblings. The a-wave is a measurement of outer retinal function, signifying the activation here of cone photoreceptors, whereas the b-wave is a measurement of activation of ON bipolar cells of the inner retina.[20,69] The zebrafish *emc1*$^{-/-}$ knockout has a small a-wave and lacks a b-wave. Comparing this to retinal histology, some of the cone photoreceptors have failed to elaborate full-length photoreceptor outer segments; however, these appear to be partially functional, with the ability to bind photons of light and hyperpolarize the cones eliciting a smaller a-wave. The loss of the b-wave signifies the inability of the electrical signal to pass to the ON bipolar cells, which could occur pre- or post-synaptically, but warrants exploration in future studies. It should be noted that the negative a-wave is often difficult to distinguish from the b-wave in larvae at this developmental stage.[70] In our study, we performed the first comprehensive assessment of visual behavior in an Emc1 knockout animal, revealing severely impaired OKR phenotypes, corroborated by severely diminished ERG retinal function and VMR locomotor behavior.

Loss of EMC1 has been linked to the retinal dystrophy retinitis pigmentosa.[14] In *Drosophila*, retinal cell-specific knockout of *emc1* leads to retinal cell death,[63] and the mouse rod-specific knockout displays progressive retinal thinning.[50] We add to this knowledge by determining that the defect in retinal thickness was predominantly found in the photoreceptor layer, which was significantly thinner in *emc1*$^{-/-}$ zebrafish. Follow-up studies using electron and confocal microscopy confirm that the thinner photoreceptor layer is due to OS reduction in and not cell body loss. The GCL layer (containing the nuclei of these cells) appeared thinner but was not statistically different. The smaller reduction observed in the IPL was. The inner plexiform layer contains dense fibrils formed by interlaced dendrites of RGCs and cell bodies of bipolar cells, horizontal cells, and amacrine cells. Therefore the reduction may mean one or all those cell types are disrupted in *emc1* knockouts. Using cell-specific knockdowns in *Drosophila*, glial cells were implicated as the primary cell type where dysfunction occurred after the loss of EMC1.[16] In *emc1*$^{-/-}$ zebrafish, however, the morphological and physiological defects observed were more selective for photoreceptor neurons. The other cell layers, including the inner nuclear layer where the cell bodies of Müller glia reside, were not significantly thinner, and the morphology of Müller glia based on Uw-55 labeling did not change. Further investigations are needed to determine if more subtle defects in the morphology or function of the Müller glia are altered. Other glial populations (astrocytes/ microglia) were not investigated in our study. Assessment for pyknotic nuclei revealed no direct evidence of increased photoreceptor death in *emc1*$^{-/-}$ mutants. However, the vacuoles present in the photoreceptor layer suggest an unhealthy photoreceptor microenvironment.

Our investigation uncovered that the loss of *emc1* had selective effects on ocular development suggesting a potentially higher expression level in photoreceptors for this gene; however, using scRNAseq databases, we did not find a corresponding increased expression of *emc1* in photoreceptors compared to other retinal cells. Previously, the *pob* (*emc3*$^{-/-}$) zebrafish mutant exhibited red cone photoreceptor degeneration albeit that *emc3* is widely expressed in the retina and the entire zebrafish. Therefore, we found another EMC protein linked to photoreceptor degeneration that is expressed widely across tissues but presents with specific ocular defects. We speculate that photoreceptors may be highly sensitive to membrane protein synthesis defects due to the high abundance of these proteins in these specialized neuronal cells. Correct folding by EMC of these membrane proteins is important for photoreceptor function. 90% of mutations in opsin genes associated with retinal degeneration cause impairments in protein folding.[71] The correct synthesis and transport of these membrane proteins are therefore critical steps for photoreceptor outer segment maturation. We speculate that when *emc1* is mutated, protein folding is disrupted leading to defects in the outer segment and photoreceptor function.

Within photoreceptors, the outer segment is the cell structure most reported to be affected after loss of EMC1. Using electron microscopy and immunofluorescent methods we show that the morphology and appearance of the outer segments were reduced across the *emc1*$^{-/-}$ retina. The appearance and localization of outer segment enriched proteins such as rhodopsin, Rab28, and peripherin were significantly limited in *emc1*$^{-/-}$. This supports the role of EMC1 in photoreceptor outer segment protein biogenesis.[10,11,50] Many other proteins in the photoreceptors tested in this study including Gnb3 (membrane-associated) and centrin (connecting cilium) were disrupted in terms of expression levels or localization in *emc1*$^{-/-}$ so it remains unclear if only outer segment proteins are specifically affected or if the loss of *emc1* has broader effects on protein synthesis in photoreceptors.

Our results reveal that loss of *emc1* in zebrafish larvae leads to abnormalities in the development of the hyaloid vasculature (HV), with disorganized and detached hyaloid vessels. These findings are consistent with recent reports linking EMC1 dysfunction to retinal vascular abnormalities, particularly in conditions such as familial exudative vitreoretinopathy (FEVR).[72] Perturbed vasculature growth and density in the retina were observed in the mouse endothelial cell-specific knockout of Emc1.[45] HV defects in the *emc1*$^{-/-}$ larvae mirror the irregular vascularization seen in EMC1-related FEVR, suggesting that mutations to *emc1* disrupt critical pathways involved in vascular development and stability within the eye. In contrast, *emc1*$^{-/-}$ did not appear to affect the formation of intersegmental vessels (ISV) in the trunk, highlighting the potential specificity of *emc1*'s role in ocular vasculature. Our findings contribute to a growing body of evidence that underscores the significance of EMC1 in the molecular mechanisms underlying FEVR and similar retinal vascular disorders. Further research is needed to explore the therapeutic potential of targeting EMC1 pathways to mitigate these vascular abnormalities.

Our transcriptomic analysis demonstrates for the first time that the expression of genes involved in phototransduction is significantly reduced in *emc1*$^{-/-}$. Indeed, both types of photoreceptors are affected, as genes belonging to the transduction cascades in both rods (e.g., *gnat1, rho, grk1a*) and cones (e.g., *gnat2, opn1mw1, opn1sw1*) were significantly reduced in the absence of Emc1. This is consistent with the reduced protein levels of Gnat1, Grk1, and Pde6b observed via immunoblotting in the mouse Emc1 rod-specific knockout and the reduced immunolabeling of M and S-opsin observed in the mouse Emc1 cone-specific knockout.[50] Previous transcriptomic and proteomic analyses in human retinal microvascular endothelial cells (HRECs) and Xenopus linked the loss of EMC1/*emc1* to a decrease in Wnt signaling.[45,61] In this study, pathway analysis of differentially expressed genes (DEGs) in zebrafish *emc1*$^{-/-}$, did not identify Wnt signaling as a significantly dysregulated pathway. Therefore, we inspected the DEG list for individual Wnt pathway genes, for example, *wnt, dkk1a, fzd4*, but these were not differentially expressed at the transcript level in *emc1*$^{-/-}$ eyes. Finally, the expression of *axin2*, a readout marker of Wnt signaling pathway, was assessed by qPCR from 5 dpf zebrafish larvae and there was no statistical difference between siblings and *emc1*$^{-/-}$ (1 vs. 1.124 ± 0.256, data not shown). Hence, in zebrafish, defective Wnt signaling does not appear to be a key molecular mechanism of action behind the loss of *emc*1.

Previous studies presented conflicting results about whether the loss of EMC1 leads to ER stress. In *C. elegans*, the knockdown of EMC subunits, including *emc1*, triggered the unfolded protein response (UPR).[9] In contrast, ER stress protein levels (e.g., Eif2, Atf6, Chop) were not significantly different in the mouse Emc1 rod-specific knockout.[50] Our transcriptomic profiling identified that the expression of genes related to ER stress (e.g., *eif2ak3, atf6, ddit3*(chop)) was significantly increased in *emc1*$^{-/-}$, supporting a role for UPR activation in zebrafish eyes lacking *emc1*. The increase in expression of aminoacyl t-amine synthetases (*yars1, tars1, and nars1*) may be a sign of compensatory mechanisms in the cells to maintain protein synthesis. It is interesting to note that the gain of function of some of these genes is linked to neurodegenerative disorders.[73,74] KEGG Pathway analysis of the upregulated DEGs in *emc1*$^{-/-}$ found a significant KEGG pathway linked to the immune system; *"cytokine-receptor interaction"*. The increase in proinflammatory chemo/cytokines (e.g., *ccl20, lepa, and il12a*), interferon regulatory factors (e.g., *irf3 and irf9*), and receptors (e.g., *cxcr3, il12r, and tnfrsfr9*a) indicates inflammation is induced in the *emc1*$^{/-}$ retina. Further work needs to characterize this phenotype and elucidate whether there is an infiltration of immune cells into the retina.

In conclusion, our study confirmed the fundamental role of Emc1 in vision and ocular development. Emc1 is required for establishing the unique morphology of the outer segments of photoreceptors, by facilitating photoreceptor protein synthesis and localization. Emc1 dysregulation also impacts the development of retinal vasculature. These morphological phenotypes were associated with a decrease in the expression of genes related to phototransduction and increases in genes related to ER stress.

AUTHOR CONTRIBUTIONS

T.M., H.S., A.L.R., and B.N.K. conceptualization; T.M. data curation; T.M, C.W., N.R., Y.A., and B.N.K. formal analysis; T.M., C.W., A.L.R., H.S., and B.N.K. Validation. T.M., C.W., A.L.R, H.S., and Y.A. investigation. T.M., A.M., and B.N.K. methodology; T.M. and B.N.K. writing-original draft. B.N.K. resources; B.N.K. supervision; B.N.K. project administration; R.C. B.S.R, and Y.A. created the original genetic models. H.S. and S.C. collected all samples for whole genome and RNA sequencing, T.M. and C.W. generated the transgenic models in the knockout background. C.W. performed visual function analysis and light microscopy. A.L.R. performed ERG analysis and T.E.M., T.M., and A.L.R. performed immunohistochemistry and confocal imaging. T.M., C.W., and Y.A., performed fluorescent microscopy. M.R.S. and M.A.E. performed RNA sequencing and analysis, and candidate SNP analysis. A.S. provided intellectual input, supervision, and resources for RNA-seq and SNP analysis. S.V. performed the whole genome sequencing analysis. T.M. performed RNA sequencing and pathway analysis. T.M., A.L.R., Y.A., and B.N.K. interpreted the results and provided significant intellectual input.

ACKNOWLEDGMENTS

We thank the UCD Conway Institute Imaging Core Facilities, namely Ms. Tiina O′ Neill, Dr. Dimitri Scholz, and Dr. Niamh Stephens for imaging support and services and the UCD Conway Instititute Genomic Core Facilities, namely Ms. Catherine Moss, Dr. Kevin Byrne, and Dr. Matthias Wilm for training and support. We also thank the Biomedical Facility UCD for maintenance of zebrafish stocks. Antibodies are kindly supplied by J. Fadool (Florida State University), M. Ader, and J. Saari (University of Washington). Graphical abstract created in BioRender. Open access funding provided by IReL.

FUNDING INFORMATION

Science Foundation Ireland under grant number 20/FFP-P/8538 and 04/IN3/B559. TopMed10—Marie Skłodowska-Curie Actions COFUND Program: European Union's Horizon 2020 research and innovation program under the Marie Skłodowska-Curie grant agreement No. 666010 to H.S. National Eye Institute Intramural Research Program Z01EY000450 to A.S.

DISCLOSURES

The authors declare that the research was conducted in the absence of any commercial or financial relationships that could be construed as a potential conflict of interest.

DATA AVAILABILITY STATEMENT

Raw data supporting the findings of this study are available from the corresponding author on request.

ORCID

Tess McCann https://orcid.org/0009-0006-2206-6221
Husvinee Sundaramurthi https://orcid.org/0000-0002-0041-0451
Ciara Walsh https://orcid.org/0000-0002-7873-5627
Sanamjeet Virdi https://orcid.org/0000-0002-3122-9954
Yolanda Alvarez https://orcid.org/0000-0002-7483-6279
Beata Sapetto-Rebow https://orcid.org/0009-0004-5107-4461
Ross F. Collery https://orcid.org/0000-0002-1550-299X
Stephen P. Carter https://orcid.org/0000-0002-0562-8783
Ailis Moran https://orcid.org/0000-0002-8706-9777
Ruth Mulholland https://orcid.org/0009-0003-7838-3996
John J. O'Connor https://orcid.org/0000-0001-8229-8602
Michael R. Taylor https://orcid.org/0000-0003-0848-4620
Nora Rauch https://orcid.org/0000-0001-6009-5177
Margaret R. Starostik https://orcid.org/0000-0002-5274-2765
Milton A. English https://orcid.org/0009-0001-0146-8049
Anand Swaroop https://orcid.org/0000-0002-1975-1141
Robert Geisler https://orcid.org/0000-0002-3909-8311
Alison L. Reynolds https://orcid.org/0000-0002-3147-0094
Breandán N. Kennedy https://orcid.org/0000-0001-7991-4689

REFERENCES

1. Georgiou M, Fujinami K, Michaelides M. Inherited retinal diseases: therapeutics, clinical trials and end points-a review. *Clin Experiment Ophthalmol*. 2021;49:270-288.
2. Bujakowska KM, Liu Q, Pierce EA. Photoreceptor cilia and retinal ciliopathies. *Cold Spring Harb Perspect Biol*. 2017;9(10):a028274.
3. Molday RS, Moritz OL. Photoreceptors at a glance. *J Cell Sci*. 2015;128:4039-4045.
4. Moran AL, Fehilly JD, Floss Jones D, Collery R, Kennedy BN. Regulation of the rhythmic diversity of daily photoreceptor outer segment phagocytosis in vivo. *FASEB J*. 2022;36:e22556.
5. Faber S, Roepman R. Balancing the photoreceptor proteome: Proteostasis network therapeutics for inherited retinal disease. *Genes*. 2019;10(8):557.
6. Richardson R, Tracey-White D, Webster A, Moosajee M. The zebrafish eye—a paradigm for investigating human ocular genetics. *Eye*. 2016;31:68-86.
7. Collery RF, Cederlund ML, Smyth VA, Kennedy BN. Applying transgenic zebrafish technology to study the retina. *Adv Exp Med Biol*. 2006;572:201-207.
8. Chhetri J, Jacobson G, Gueven N. Zebrafish—on the move towards ophthalmological research. *Eye*. 2014;28:367-380.

9. Richard M, Boulin T, Robert VJP, Richmond JE, Bessereau J-L. Biosynthesis of ionotropic acetylcholine receptors requires the evolutionarily conserved ER membrane complex. *Proc Natl Acad Sci*. 2013;110:E1055-E1063.
10. Satoh T, Ohba A, Liu Z, Inagaki T, Satoh AK. dPob/EMC is essential for biosynthesis of rhodopsin and other multi-pass membrane proteins in drosophila photoreceptors. *elife*. 2015;4:e06306.
11. Shurtleff MJ, Itzhak DN, Hussmann JA, et al. The ER membrane protein complex interacts cotranslationally to enable biogenesis of multipass membrane proteins. *elife*. 2018;7:e37018.
12. Guna A, Volkmar N, Christianson JC, Hegde RS. The ER membrane protein complex is a transmembrane domain insertase. *Science*. 2018;359:470-473.
13. Chitwood PJ, Juszkiewicz S, Guna A, Shao S, Hegde RS. EMC is required to initiate accurate membrane protein Topogenesis. *Cell*. 2018;175:1507-1519.e16.
14. Abu-Safieh L, Alrashed M, Anazi S, et al. Autozygome-guided exome sequencing in retinal dystrophy patients reveals pathogenetic mutations and novel candidate disease genes. *Genome Res*. 2013;23:236-247.
15. Harel T, Yesil G, Bayram Y, et al. Monoallelic and Biallelic variants in EMC1 identified in individuals with global developmental delay, Hypotonia, scoliosis, and cerebellar atrophy. *Am J Hum Genet*. 2016;98:562-570.
16. Chung H-L, Rump P, Lu D, et al. De novo variants in EMC1 lead to neurodevelopmental delay and cerebellar degeneration and affect glial function in drosophila. *Hum Mol Genet*. 2022;31:3231-3244.
17. Sapetto-Rebow B, McLoughlin SC, O'Shea LC, et al. Maternal topoisomerase II alpha, not topoisomerase II beta, enables embryonic development of zebrafish top2a−/− mutants. *BMC Dev Biol*. 2011;11:71.
18. Deeti S, O'Farrell S, Kennedy BN. Early safety assessment of human oculotoxic drugs using the zebrafish visualmotor response. *J Pharmacol Toxicol Methods*. 2014;69:1-8.
19. Gómez Sánchez A, Álvarez Y, Colligris B, Kennedy BN. Affordable and effective optokinetic response methods to assess visual acuity and contrast sensitivity in larval to juvenile zebrafish. *Open Res Eur*. 2021;1:92.
20. Makhankov YV, Rinner O, Neuhauss SCF. An inexpensive device for non-invasive electroretinography in small aquatic vertebrates. *J Neurosci Methods*. 2004;135:205-210.
21. Wong KY, Gray J, Hayward CJC, Adolph AR, Dowling JE. Glutamatergic mechanisms in the outer retina of larval zebrafish: analysis of electroretinogram b- and d-waves using a novel preparation. *Zebrafish*. 2004;1:121-131.
22. Uribe RA, Gross JM. Immunohistochemistry on cryosections from embryonic and adult zebrafish eyes. *CSH Protoc*. 2007;2007:db.prot4779.
23. Joshi S, Virdi S, Etard C, Geisler R, Strähle U. Mutation of a serine near the catalytic site of the choline acetyltransferase a gene almost completely abolishes motility of the zebrafish embryo. *PLoS One*. 2018;13:e0207747.
24. Bolger AM, Lohse M, Usadel B. Trimmomatic: a flexible trimmer for Illumina sequence data. *Bioinformatics*. 2014;30:2114-2120.
25. Ewels P, Magnusson M, Lundin S, Käller M. MultiQC: summarize analysis results for multiple tools and samples in a single report. *Bioinformatics*. 2016;32:3047-3048.
26. Dobin A, Davis CA, Schlesinger F, et al. STAR: ultrafast universal RNA-seq aligner. *Bioinformatics*. 2013;29:15-21.
27. Bray NL, Pimentel H, Melsted P, Pachter L. Near-optimal probabilistic RNA-seq quantification. *Nat Biotechnol*. 2016;34:525-527.
28. Soneson C, Love MI, Robinson MD. Differential analyses for RNA-seq: transcript-level estimates improve gene-level inferences. *F1000Res*. 2015;4:1521.
29. Ritchie ME, Phipson B, Wu D, et al. Limma powers differential expression analyses for RNA-sequencing and microarray studies. *Nucleic Acids Res*. 2015;43:e47.
30. Leek JT. Svaseq: removing batch effects and other unwanted noise from sequencing data. *Nucleic Acids Res*. 2014;42:e161.
31. Robinson MD, Smyth GK. Moderated statistical tests for assessing differences in tag abundance. *Bioinformatics*. 2007;23:2881-2887.
32. Robinson MD, Oshlack A. A scaling normalization method for differential expression analysis of RNA-seq data. *Genome Biol*. 2010;11:R25.
33. Robinson MD, McCarthy DJ, Smyth GK. edgeR: a Bioconductor package for differential expression analysis of digital gene expression data. *Bioinformatics*. 2010;26:139-140.
34. Hill JT, Demarest BL, Bisgrove BW, Gorsi B, Su Y-C, Yost HJ. MMAPPR: mutation mapping analysis pipeline for pooled RNA-seq. *Genome Res*. 2013;23:687-697.
35. Daly C, Shine L, Heffernan T, et al. A brain-derived neurotrophic factor mimetic is sufficient to restore cone photoreceptor visual function in an inherited blindness model. *Sci Rep*. 2017;7:11320.
36. Ward R, Kaylor JJ, Cobice DF, et al. Non-photopic and photopic visual cycles differentially regulate immediate, early, and late phases of cone photoreceptor-mediated vision. *J Biol Chem*. 2020;295:6482-6497.
37. Blanks JC, Johnson LV. Specific binding of peanut lectin to a class of retinal photoreceptor cells. A species comparison. *Invest Ophthalmol Vis Sci*. 1984;25:546-557.
38. Nadolski NJ, Balay SD, Wong CXL, Waskiewicz AJ, Hocking JC. Abnormal cone and rod photoreceptor morphogenesis in gdf6a mutant zebrafish. *Invest Ophthalmol Vis Sci*. 2020;61:9.
39. Muto A, Orger MB, Wehman AM, et al. Forward genetic analysis of visual behavior in zebrafish. *PLoS Genet*. 2005;1:e66.
40. Pleiner T, Hazu M, Pinton Tomaleri G, Nguyen VN, Januszyk K, Voorhees RM. A selectivity filter in the ER membrane protein complex limits protein misinsertion at the ER. *J Cell Biol*. 2023;222(8):e202212007.
41. Zhu Q, Zhu X, Zhang L. ER membrane complex (EMC): structure, functions, and roles in diseases. *FASEB J*. 2024;38:e23539.
42. Miller-Vedam LE, Bräuning B, Popova KD, et al. Structural and mechanistic basis of the EMC-dependent biogenesis of distinct transmembrane clients. *elife*. 2020;9:e62611.
43. Taylor MR, Kikkawa S, Diez-Juan A, et al. The zebrafish pob gene encodes a novel protein required for survival of red cone photoreceptor cells. *Genetics*. 2005;170:263-273.
44. Hoang T, Wang J, Boyd P, et al. Gene regulatory networks controlling vertebrate retinal regeneration. *Science*. 2020;370(6519):eabb8598.
45. Li S, Yang M, Zhao R, et al. Defective EMC1 drives abnormal retinal angiogenesis via Wnt/β-catenin signaling and may be associated with the pathogenesis of familial exudative vitreoretinopathy. *Genes Dis*. 2023;10:2572-2585.
46. Lawson ND, Weinstein BM. In vivo imaging of embryonic vascular development using transgenic zebrafish. *Dev Biol*. 2002;248:307-318.

47. Alvarez Y, Cederlund ML, Cottell DC, et al. Genetic determinants of hyaloid and retinal vasculature in zebrafish. *BMC Dev Biol*. 2007;7:114.
48. Jonikas MC, Collins SR, Denic V, et al. Comprehensive characterization of genes required for protein folding in the endoplasmic reticulum. *Science*. 2009;323:1693-1697.
49. Tian S, Wu Q, Zhou B, et al. Proteomic analysis identifies membrane proteins dependent on the ER membrane protein complex. *Cell Rep*. 2019;28:2517-2526.e5.
50. Li X, Jiang Z, Su Y, et al. Deletion of Emc1 in photoreceptor cells causes retinal degeneration in mice. *FEBS J*. 2023;290:4356-4370.
51. Carter SP, Moran AL, Matallanas D, McManus GJ, Blacque OE, Kennedy BN. Genetic deletion of zebrafish Rab28 causes defective outer segment shedding, but not retinal degeneration. *Front Cell Dev Biol*. 2020;8:136.
52. Maurer-Stroh S, Koranda M, Benetka W, Schneider G, Sirota FL, Eisenhaber F. Towards complete sets of farnesylated and geranylgeranylated proteins. *PLoS Comput Biol*. 2007;3:e66.
53. Goldberg AFX. Role of peripherin/rds in vertebrate photoreceptor architecture and inherited retinal degenerations. *Int Rev Cytol*. 2006;253:131-175.
54. Lu Z, Hu X, Reilly J, et al. Deletion of the transmembrane protein Prom1b in zebrafish disrupts outer-segment morphogenesis and causes photoreceptor degeneration. *J Biol Chem*. 2019;294:13953-13963.
55. Lee RH, Lieberman BS, Yamane HK, Bok D, Fung BK. A third form of the G protein beta subunit. 1. Immunochemical identification and localization to cone photoreceptors. *J Biol Chem*. 1992;267:24776-24781.
56. Ritchey ER, Bongini RE, Code KA, Zelinka C, Petersen-Jones S, Fischer AJ. The pattern of expression of guanine nucleotide-binding protein beta3 in the retina is conserved across vertebrate species. *Neuroscience*. 2010;169:1376-1391.
57. Stemerdink M, Broekman S, Peters T, Kremer H, de Vrieze E, van Wijk E. Generation and characterization of a zebrafish model for ADGRV1-associated retinal dysfunction using CRISPR/Cas9 genome editing technology. *Cells*. 2023;12(12):1598.
58. Geetha TS, Lingappa L, Jain AR, et al. A novel splice variant in EMC1 is associated with cerebellar atrophy, visual impairment, psychomotor retardation with epilepsy. *Mol Genet Genomic Med*. 2018;6:282-287.
59. Homsy J, Zaidi S, Shen Y, et al. De novo mutations in congenital heart disease with neurodevelopmental and other congenital anomalies. *Science*. 2015;350:1262-1266.
60. Jin SC, Homsy J, Zaidi S, et al. Contribution of rare inherited and de novo variants in 2,871 congenital heart disease probands. *Nat Genet*. 2017;49:1593-1601.
61. Marquez J, Criscione J, Charney RM, et al. Disrupted ER membrane protein complex-mediated topogenesis drives congenital neural crest defects. *J Clin Invest*. 2020;130:813-826.
62. Cao X, An J, Cao Y, et al. EMC3 is essential for retinal organization and neurogenesis during mouse retinal development. *Invest Ophthalmol Vis Sci*. 2021;62:31.
63. Xiong L, Zhang L, Yang Y, et al. ER complex proteins are required for rhodopsin biosynthesis and photoreceptor survival in drosophila and mice. *Cell Death Differ*. 2020;27:646-661.
64. Zhu X, Qi X, Yang Y, et al. Loss of the ER membrane protein complex subunit Emc3 leads to retinal bipolar cell degeneration in aged mice. *PLoS One*. 2020;15:e0238435.
65. Sun K, Liu L, Jiang X, et al. The endoplasmic reticulum membrane protein complex subunit Emc6 is essential for rhodopsin localization and photoreceptor cell survival. *Genes Dis*. 2024;11:1035-1049.
66. Bilotta J, Saszik S, Sutherland SE. Rod contributions to the electroretinogram of the dark-adapted developing zebrafish. *Dev Dyn*. 2001;222:564-570.
67. Branchek T. The development of photoreceptors in the zebrafish, brachydanio rerio. II. Function. *J Comp Neurol*. 1984;224:116-122.
68. Branchek T, Bremiller R. The development of photoreceptors in the zebrafish, Brachydanio rerio. I. Structure. *J Comp Neurol*. 1984;224:107-115.
69. Dowling JE. *The Retina: An Approachable Part of the Brain*. Harvard University Press; 1990.
70. Chrispell JD, Rebrik TI, Weiss ER. Electroretinogram analysis of the visual response in zebrafish larvae. *J Vis Exp*. 2015;(97):52662.
71. Bighinati A, Adani E, Stanzani A, D'Alessandro S, Marigo V. Molecular mechanisms underlying inherited photoreceptor degeneration as targets for therapeutic intervention. *Front Cell Neurosci*. 2024;18:1343544.
72. Le V, Abdelmessih G, Dailey WA, et al. Mechanisms underlying rare inherited pediatric retinal vascular diseases: FEVR, Norrie disease, persistent fetal vascular syndrome. *Cells*. 2023;12(21):2579.
73. Boczonadi V, Jennings MJ, Horvath R. The role of tRNA synthetases in neurological and neuromuscular disorders. *FEBS Lett*. 2018;592:703-717.
74. Wei N, Zhang Q, Yang X-L. Neurodegenerative Charcot-Marie-tooth disease as a case study to decipher novel functions of aminoacyl-tRNA synthetases. *J Biol Chem*. 2019;294:5321-5339.

How to cite this article: McCann T, Sundaramurthi H, Walsh C, et al. Emc1 is essential for vision and zebrafish photoreceptor outer segment morphogenesis. *The FASEB Journal*. 2024;38:e70086. doi:10.1096/fj.202401977R